Parameter Estimation of Gravitational Waves from Nonprecessing BH-NS Inspirals with higher harmonics:

Comparing MCMC posteriors to an Effective Fisher Matrix

Richard O'Shaughnessy¹,* Ben Farr², Evan Ochsner¹, Hee-Suk Cho³, Chunglee Kim^{4,5,6},† and Chang-Hwan Lee³

¹Center for Gravitation and Cosmology, University of Wisconsin-Milwaukee, Milwaukee, WI 53211, USA

²Center for Interdisciplinary Exploration and Research in Astrophysics (CIERA) & Dept. of Physics and Astronomy,

Northwestern University, 2145 Sheridan Rd, Evanston, IL 60208, USA.

³Department of Physics, Pusan National University, Busan 609-735, Korea

⁴ Astronomy Program, Department of Physics and Astronomy,

Seoul National University, 1 Gwanak-ro, Gwanak-gu, Seoul 151-742, Korea

⁵Korea Institute of Science and Technology Information, Daejeon 305-806, Korea and

⁶Department of Physics, West Virginia University, PO Box 6315, Morgantown, WV 26505, USA

(Dated: February 24, 2014)

Most calculations of the gravitational wave signal from merging compact binaries limit attention to the leading-order quadrupole when constructing models for detection or parameter estimation. Some studies have claimed that if additional "higher harmonics" are included consistently in the gravitational wave signal and search model, binary parameters can be measured much more precisely. Using the lalinference Markov-chain Monte Carlo parameter estimation code, we construct posterior parameter constraints associated with two distinct nonprecessing black hole-neutron star (BH-NS) binaries, each with and without higher-order harmonics. All simulations place a plausible signal into a three-detector network with Gaussian noise. Our simulations suggest that higher harmonics provide little information, principally allowing us to measure a previously unconstrained angle associated with the source geometry well but otherwise improving knowledge of all other parameters by a few percent for our loud fiducial signal ($\rho = 20$). Even at this optimistic signal amplitude, different noise realizations have a more significant impact on parameter accuracy than higher harmonics. We compare our results with the "effective Fisher matrix" introduced previously as a method to obtain robust analytic predictions for complicated signals with multiple significant harmonics. We find generally good agreement with these predictions; confirm that intrinsic parameter measurement accuracy is nearly independent of detector network geometry; and show that uncertainties in extrinsic and intrinsic parameters can to a good approximation be separated. For our fiducial example, the individual masses can be determined to lie between $7.11-11.48M_{\odot}$ and $1.77-1.276M_{\odot}$ at greater than 99% confidence, accounting for unknown BH spin. Assuming comparable control over waveform systematics, measurements of BH-NS binaries can constrain the BH and perhaps NS mass distributions. Using analytic arguments to guide extrapolation, we anticipate higher harmonics should provide little new information about nonprecessing BH-NS binaries, for the signal amplitudes expected for the first few detections. Though our study focused on one particular example – higher harmomics – any study of subdominant degrees of freedom in gravitational wave astronomy can adopt the tools presented here (V/V_{prior}) and D_{KL} to assess whether new physics is accessible (e.g., modifications of gravity; spin-orbit misalignment) and if so precisely what information those new parameters provide.

PACS numbers: 04.30.-w, 04.80.Nn, 95.55.Ym

Contents

| I. Introduction | 2 |
|---|---|
| A. Context and prior work | 3 |
| B. Executive summary and outline | 3 |
| II. Waveforms and coordinate choices | 5 |
| A. Compact binary waveform model | 5 |
| B. Fiducial binary and detector network | 5 |
| C. The importance of coordinate choices | 6 |

| III. | Parameter estimation methods | 7 |
|---------------|---|----|
| | A. Bayes' theorem for GW parameter estimation | 7 |
| | B. MCMC parameter estimation: lalinference_mcmc | 8 |
| | C. Prior volume ratio | 9 |
| | D. Comparing two distributions' shapes | 10 |
| | E. Quantifying multidimensional correlations | 12 |
| | F. Bounded parameters and truncated distributions | 12 |
| IV. | Parameter estimation results | 12 |
| | A. Intrinsic distributions agree | 14 |
| | B. Marginal information from higher harmonics is confined to source orientation | 15 |
| | C. Bounding the relative impact of higher harmonics | 16 |
| | D. Posteriors separate into intrinsic and extrinsic variables, after maximizing in time and phase | 19 |
| V. | Comparing parameter estimation to the effective Fisher matrix | 20 |
| | A. Effective Fisher matrix predictions | 20 |
| | B. Comparing predicted and calculated intrinsic parameter distributions | 20 |
| | C. Geometric parameters | 21 |
| VI. | Generalizing the results | 23 |
| VII. | Conclusions | 24 |
| Α. | Comparing two distributions' shapes | 25 |
| В. | Sensitivity to PN model, sampling rate and starting frequency | 26 |
| $\mathbf{C}.$ | Effective dimension and prior volume versus signal amplitude | 26 |
| | 1. Review of parallel tempering and thermodynamic integration | 26 |
| | 2. Effective dimension versus amplitude | 28 |
| | Acknowledgments | 29 |
| | References | 29 |

I. INTRODUCTION

Ground based gravitational wave detector networks (notably LIGO [1] and Virgo [2]) are sensitive to the relatively well understood signal from the lowest-mass compact binaries $M = m_1 + m_2 \le 16 M_{\odot}$ [3–14]. Strong signals permit high-precision constraints on binary parameters, particularly when the binary precesses. When interpreting plausible data from ground-based instruments via Bayesian inference, a detailed model for these constraints can require the simulation of tens of millions of binary waveforms, to adequately sample the high-dimensional model space [15–21]. The results of these calculations is a model for a strongly correlated, often highly multimodal, and generically broadly-distributed posterior in 15 dimensions. A simple procedure to reliably estimate the performance of these detailed calculations is critical, to interpret and communicate their results; to validate the estimate itself; and to allow the broader astrophysical community to predict how informative future gravitational wave surveys will be.

One general algorithm is widely used to estimate the performance of these detailed calculations: the Fisher in-

formation matrix [22–26]. Derived as a locally Gaussian approximation to the posterior, the Fisher matrix approximation is expected to work well when observations provide tight constraints on all parameters [27]. When valid, this easily-understood and calculated approximation can be applied both to simple test problems and to the full multi-detector likelihood, by incorporating information about detector network geometry [28]. Repeated theoretical and practical investigations, however, have suggested the Fisher matrix must be calculated with care, to avoid numerical pathologies (e.g., associated with the sampling rate of the signal; see Cho et al. [22], henceforth denoted COOKL); used with care, as it becomes ill-conditioned and numerically unstable in the presence of strong degeneracies; and applied with care, only to sources in the appropriate "strong-signal" limit [27].

COOKL implicitly proposed three idealizations which, together, convert the Fisher matrix to a more robust low-dimensional calculation, particularly for nonprecessing binaries. First and foremost, for strong sources with well-localized sky locations, *ignore* the sky location parameters: these (and other) extrinsic, geometrical parameters almost perfectly separate from intrinsic parame-

ters.¹ Second, for nonprecessing sources, assume the network has nearly equal sensitivity to both polarizations: only for a handful of source orientations will asymmetric preferential sensitivity to one polarization or another bias our conclusions about *intrinsic* parameters. Finally, this paper pioneered an "effective Fisher matrix" approach, eliminating observationally irrelevant scales by suitably smoothing the local ambiguity function. Using these approximations, COOKL provided concrete predictions for the performance of Bayesian parameter estimation codes, for three selected cases.

In this work, we compare these predictions against direct and comprehensive Bayesian parameter estimation methods which, by systematically comparing all possible candidate signals to data, construct a posterior probability distribution [15–21]. Despite the considerable idealizations involved, the predictions of COOKL work surprisingly well. Moreover, by repeated concrete calculations, we corroborate their conclusions about the information communicated via higher harmonics from BH-NS binaries.

Even for nonprecessing binaries inspiralling along a quasicircular orbit, the gravitational wave signal from merging compact binaries remains surprisingly complicated, as source multipoles contribute to the gravitational wave signal, at several different harmonics of the orbital frequency. Though the gravitational mass quadrupole dominates, these remaining "higher harmonics" influence the accessible signal, contributing noticeably to the overall signal amplitude and influencing parameter estimation accuracy [22, 29]. Using concrete examples, COOKL argued that while higher harmonics do provide additional information about BH-NS binaries, for observationally plausible signal amplitudes that information is principally geometric, encoding the source orientation relative to the line of sight, and does not significantly improve the measurement of intrinsic parameters (masses and spins) for BH-NS binaries.

A. Context and prior work

In the context of ground-based detectors, some studies outside and within the LIGO scientific collaboration have compared the predictions of the Fisher matrix to parameter recovery strategies, including maximum likelihood [23–25, 30] and detailed MCMC calculations. Usually, these studies investigate measurement error, using large-scale simulations to determine (for example) how often the maximum-likelihood point lies within the predicted confidence intervals derived from a Fisher matrix or MCMC prediction. In this paper, we emphasize a related problem: modeling the *shape* of the posterior prob-

ability distribution. Specifically, we compare two distributions by first (implicitly) translating both to a common point, each centered on their maximum-likelihood value. Since this shift is explicitly coordinate dependent, we perform the shift and comparison in a handful of phenomenologically-motivated coordinate systems. Once translated, we evaluate the covariance matrix for each distribution, then compare them. We similarly compare the covariance matrix against predictions from COOKL. We do not modify our procedure to account for edge effects, e.g. from the upper bound on the mass ratio or black hole spin.

To determine the shape of each posterior, as noted above, we employ the lalsimulation and lalinference [15, 31] code libraries developed by the LIGO Scientific Collaboration and Virgo collaboration. The former generates gravitational waveforms using several state-of-theart signal models and the latter uses Bayesian inference techniques to analyze gravitational-wave detector data for parameter estimation and model selection purposes.

We adopt fiducial initial LIGO and Virgo detector models both for efficiency and for comparison with the results in COOKL. The next generation of gravitational wave detector networks will be sensitive to lower frequencies, leading to significantly longer signals. Existing parameter estimation methods are currently prohibitively computationally-expensive for these long signals. However, these existing methods have demonstrated they can reliably estimate posterior probability distributions for signals in the most recently operating generation of detectors [15]. Therefore, one of the key goals of this work is to demonstrate that the predictions of the effective Fisher matrix method are a reasonable proxy for the parameter estimation capabilities of a full Bayesian inference analysis. This will justify using the effective Fisher matrix approach to predict the parameter estimation capabilities of advanced detectors. Of course, it will be critical to enable Bayesian parameter estimation pipelines to run on the longer signals of advanced detectors, but such work is outside the scope of this paper.

As described in [22], signal models including both higher harmonics or spin have been extensively applied to parameter estimation problems for ground-based [15, 29] and space-based [32, 33] detectors. In the absence of precession, higher harmonics are known to break degeneracies and improve sky localization, particularly for LISA [33–35]. Our results suggest that higher harmonics provide little useful additional information about BH-NS binaries.

B. Executive summary and outline

In this work, we describe how well the parameters of the nonprecessing signals studied in [22] can be recovered when inserted into a realistic three-detector network, both with and without higher harmonics.

Our work builds upon a large, community-wide effort

¹ Some sources, identified electromagnetically, may already have well-determined sky locations.

to construct and validate parameter estimation strategies for ground-based gravitational-wave networks, culminating in the lalinference code [15] employed in this work. In turn, this code implements parameter estimation strategies that have previously been extensively applied to gravitational wave parameter estimation [15–21].

Using a fixed source sky location and distance, we generate random noise for each detector; insert a signal into each detector; and systematically compare the set of detector data with all plausible compact binaries in a broad prior range, allowing both the BH and NS to have spin. ² We explicitly use identical noise realizations to compare signals with and without higher harmonics, to isolate their effect on the posterior distribution and evaluate what additional information higher harmonics provide.

For the masses considered here, higher harmonics principally provide additional constraints on the source *geometry*, but not its intrinsic properties. In particular, they do not significantly improve the measurement of the masses and spins of our fiducial binary, but instead break a degeneracy between the polarization angle and orbital phase of the binary at some reference point, thereby improving the measurement of these parameters.

We use several techniques to compare the posteriors of simulations with different noise realizations to one another and to effective Fisher matrix predictions. These include a prior volume ratio, V/V_{prior} , as a measure of amount of information being extracted from the signal, a specialized version of the KL-divergence, D_{KL} , to compare the similarity of two distributions, and the mutual information, I(A,B), as a measure of the correlations between two subsets of parameters. From the prior volume, we find that the higher harmonics provide more information than would an equivalent increase in SNR, but that it is still rather modest, the change in volume being comparable to the differences between different noise realizations. From D_{KL} and inspection of marginalized posteriors, we find that simulations with different noise realizations produce posteriors that are similar to one another and to the highly idealized effective Fisher matrix predictions provided in COOKL. From the mutual information, we find that after marginalizing over time and polarization angle, there is a strong separation into intrinsic and extrinsic parameters with only very weak correlations between the two.

We also make two observations about the computational cost of Bayesian parameter estimation using amplitude-corrected waveforms. First, to perform calculations which include the low frequency portions of the higher harmonics, one needs to generate waveforms at lower orbital frequencies than for restricted waveforms.

Second, to fully resolve the highest harmonics during the late inspiral, one needs to use a higher sample rate to avoid aliasing. These effects mean that, to properly include amplitude corrections, one ostensibly needs much longer waveforms with many more samples, and this could increase the computational cost of parameter estimation by one or two orders of magnitude. Fortunately, as discussed briefly in Sec. II A, and in more detail in Appendix B, we find that doing parameter estimation on amplitude-corrected waveforms with sample rates and low frequency limits appropriate for restricted waveforms has a negligible effect on any parameter estimation results.

There are, of course, some limitations to this work. For one thing, the computational cost of waveform generation limits our MCMC computations to producing $N_{\rm eff} \simeq 10^4$ independent samples. This introduces an error $\propto 1/\sqrt{N_{\rm eff}}$ in our confidence intervals and other results. Additionally, we have only used a single post-Newtonian waveform model (SpinTaylorT4), while it is well-known there are systematic biases between different PN models [4, 36, 37]. While these errors can change specific quantitative results, they will not affect our qualitative conclusions that higher harmonics will provide a small improvement to the measurement of some extrinsic parameters but essentially no improvement to the measurement of intrinsic parameters for BH-NS binaries, and that the effective Fisher matrix method of COOKL provides a reasonably accurate prediction of the results of full Bayesian parameter estimation methods. Lastly, this work is limited to studying two physical binary systems rather than fully exploring a larger parameter space. However, by verifying this these cases in detail, we argue that the effective Fisher matrix approach can be used to efficiently explore the importance of physical effects such as spins, higher harmonics and tidal effects across any and all regions of parameter space.

Our paper is organized as follows. In Sec. II we describe the waveform model, the specific BH-NS configurations and detector network being studied, and issues related to choices of parameter space coordinates. In Sec. III we review parameter estimation via Bayes' theorem for gravitational wave data analysis, we describe the lalinference_mcmc code that is our Bayesian parameter estimation pipeline, and we introduce the quantitative techniques we will use to compare our results. In Sec. IV we examine the results of our simulations in detail, emphasizing the similarities between various results, illustrating the effect of higher harmonics, and showing how intrinsic and extrinsic parameters decouple after marginalizing over time and polarization phase. In Sec. V, we compare our simulations to the predictions of the effective Fisher matrix and argue the latter is an inexpensive proxy for the former. In Sec. VI, we argue that the binary configurations we consider are, in a sense, "typical", and we briefly discuss some implications that can be inferred for other regions of parameter space. Lastly, our conclusions can be found in Sec. VII and we

² We effectively treat both objects as black holes, a priori allowing spins up to the Kerr limit on both bodies. Due to the mass ratio ~ 7, the spin of the smaller body is suppressed by a factor ~ 49 relative to the larger body and has a negligible effect on our predictions, prior or posterior.

relegate several technical discussions to the appendices.

II. WAVEFORMS AND COORDINATE CHOICES

A. Compact binary waveform model

Following [22], we construct the post Newtonian (pN) gravitational wave signal from a BH-NS binary using the lalsimulation SpinTaylorT4 code [38]. Based on previous implementations [5, 6], this time-domain code solves the orbital dynamics of an adiabatic, quasicircular inspiralling binary using the "TaylorT4" method [4] for the phase evolution and (orbit-averaged) precession equations for the angular momenta [39]. The orbital phase and frequency evolution includes non-spinning corrections to 3.5pN order and spin corrections to 2.5pN order.³ The precession equations are given to 2pN order.

At each time, the gravitational wave signal measured by a distant observer is constructed from the orbital phase, orbital frequency and the orientations of the spins and orbital plane. The leading-order ("restricted") expression contains only the dominant second harmonic of the orbital phase. A more complete expression includes "higher harmonics" or "amplitude corrections". For quasi-circular, precessing binaries, an expression for the signal including higher harmonics is implemented in lalsimulation⁴ up to 1.5pN order [7, 39, 42].

We evolve the orbital dynamics of the binary by specifying "initial" conditions at 100 Hz, then integrating the evolution equations forwards and backwards in time. At high frequency, this binary evolution is terminated prior to merger, either when it reaches the "minimum energy circular orbit", or when the orbital frequency ceases to increase monotonically. The stopping frequencies of our injected signals (which stop due to the minimum energy condition) are shown in Table I. At low frequency, we investigated the effect of several different starting conditions, ensuring that we include the entirety of every harmonic above the lower gravitational-wave frequency cutoff of our detectors, which we take to be 30 Hz in this work. In our preferred simulations, indicated by stars (*) in Table III, the data contains the gravitational wave signal from a binary starting with a fixed initial orbital frequency of 6 Hz,⁵ low enough to guarantee all higher harmonics employed here do not begin near the detector's sensitive band. The parameter estimation strategy fixes the initial *orbital* frequency at 15 Hz in the absence of higher harmonics (only the second harmonic is present) or 6 Hz if higher harmonics (up to the fifth harmonic) are present.

Our simulations presented in the main text sample the signal at 4096 Hz. From Table I, an attentive reader may deduce that this sample rate is not sufficient to resolve the higher harmonics of the spin-aligned binary during the very late inspiral. However, the aliased portion of the signal, being higher order amplitude corrections, is suppressed by one or more powers of v, and the detectors have poor sensitivity at these high frequencies. As such, this aliasing has a negligible impact on our results. To further justify our undersampling, in Appendix B, we compare our results in the main text to results that use a higher sampling rate to eliminate aliasing. In a similar spirit, Appendix B also shows how a higher choice of lower frequency cutoff, while leaving out a portion of the higher harmonic signal, would drastically decrease the computational cost of our MCMC simulations without changing the results in any significant way.

We note that existing models of compact binary coalescences are imperfect, and there is extensive ongoing research to compute further PN corrections and construct inspiral-merger-ringdown waveforms that leverage information from numerical relativity simulations. In Appendix B, we briefly investigate how systematics from different waveform models could affect our results. Much more extensive studies of systematic errors from different waveform models can be found in [4, 36, 37], among others.

B. Fiducial binary and detector network

Following COOKL, we investigate two fiducial non-precessing binaries (one non-spinning, one spin-aligned) along a single line of sight and at a specific sky location; see Table I for the intrinsic parameters and Table II for the extrinsic parameters. For our MCMC simulations, we consider a three-detector network consisting of the first generation Hanford (H1) and Livingston (L1) LIGO detectors and the Virgo detector (V1). For each detector we use an analytic estimate of the design (one-sided) power spectral density (PSD):

$$S_{\rm H1}(f) = S_{\rm L1}(f) = 9 \times 10^{-46} \left[\left(4.49 \frac{f}{150} \right)^{-56} + 0.16 \left(\frac{f}{150} \right)^{-4.52} + 0.52 + 0.32 \left(\frac{f}{150} \right)^2 \right] , \tag{1}$$

$$S_{V1}(f) = 10.2 \times 10^{-46} \left[\left(7.87 \frac{f}{500} \right)^{-4.8} + \frac{6}{17} \frac{500}{f} + \left(\frac{f}{500} \right)^2 \right]$$
 (2)

| type | m_1 | m_2 | ι | ϕ | ϕ_{ref} | ψ | χ | $M_{\rm c}$ | η | $f_{\rm MECO}$ |
|--------------|-------------|-------------|---------|--------|-----------------------|--------|--------|-------------|--------|----------------|
| | M_{\odot} | M_{\odot} | | | | | | M_{\odot} | | $_{ m Hz}$ |
| no spin | 10 | 1.4 | $\pi/4$ | 0 | $\pi/2$ | 2.228 | 0.0 | 2.994 | 0.1077 | 559 |
| aligned spin | 10 | 1.4 | $\pi/4$ | 0 | $\pi/2$ | 2.228 | 1.0 | 2.994 | 0.1077 | 1926 |

TABLE I: Fiducial source parameters for the non-spinning and aligned-spin binaries. We adopt the chirp mass M_c and symmetric mass ratio η instead of individual masses. The orbital phase $\phi_{\rm ref}$ is defined at 100 Hz. The (constant) orbital angular momentum direction is specified by the polar angles (ι, ψ) , where the propagation direction \hat{n} is the reference axis (i.e., $\cos \iota = \hat{L} \cdot \hat{n}$). The black hole's spin is parameterized by $\chi = S_1/m_1^2$. The post-Newtonian signals used in the text terminate at a gravitational-wave frequency (of the second harmonic) $f_{\rm MECO}$, the smaller of the "minimum energy circular orbit" (hence the acronym) and the frequency at which $\dot{\omega} < 0$. The values shown are derived from the same kind of lalsimulation output used in our simulations, albeit estimated from data evaluated at a 32 kHz sampling rate for this table, rather than the 4kHz sampling rate adopted for our MCMC calculations.

| d | t | DEC | RA | Δt_{LH} | Δt_{VH} |
|-------------|-------------|--------|--------|-----------------|-----------------|
| ${\rm Mpc}$ | s | | | ms | ms |
| 23.1 | 894383679 0 | 0.5747 | 0.6485 | -3 93 | 5 98 |

TABLE II: **Source location**: Source geocenter event time and sky location. For a sense of scale, this table also provides the time differences between different detector sites, implied by that sky location and event time.

The lalinference code adopts these widely-used choices as fiducial analytic models for gaussian noise in the initial LIGO and Virgo detectors;⁶; both correspond favorably to the best reported initial detector performance [44–46]. We assume all detectors have no sensitivity below 30 Hz and follow the above formulae from 30 Hz to the Nyquist frequency. No degeneracies exist: the source location corresponds to a delay of several milliseconds between each detector pair, larger than the timing uncertainty in each interferometer. The source sky location and orientation produce a comparable signal amplitude in each interferometer; for example, for the nonspinning event, the individual detector SNRs are roughly 11.4 (H1), 14.2 (L1), and 8.66 (V1), depending on noise realization.

In each MCMC simulation, we generate a random, synthetic noise realization for each instrument such that their PSDs match Eqs. (1-2). We label different noise realizations with the value of a random seed used in their generation. To isolate the effects of different noise realizations from the more interesting effects of spin and higher harmonics, we use identical noise realizations for simulations with different injected signals. In addition, we also do noiseless simulations - that is, the data stream being analyzed is just a signal with no synthetic noise - as another baseline for comparison. When higher harmonics and/or spins were present in the signal, we performed parameter estimation with a signal model that included them; when absent, our signal model omitted them.

We also emphasize that the effective Fisher matrix results predicted in COOKL and here assume an idealized network of two co-located detectors with equal sensitivity to plus and cross polarizations and a PSD equal to $S_{\rm H1}$. Therefore, the rather good agreement between the two methods is especially encouraging considering one uses a simple, idealized network and the other a fully realistic one.

C. The importance of coordinate choices

In general, the waveform from a quasicircular compact binary is parameterized by its component masses (m_1, m_2) , the distance from binary to observer d, the time of arrival t, the orbital phase at some fiducial point in the evolution ϕ_{ref} , the orientation of its orbital angular momentum \hat{L}_N relative to the line of sight (which can be described by the inclination and polarization angles (ι, ψ)), the spin angular momenta of each body $\vec{S}_{1,2}$, and the binary's location on the observer's sky (DEC, RA). When convenient, we reparametrize the component masses in terms of the total mass $(M = m_1 + m_2)$, the symmetric mass ratio $\eta = m_1 m_2 / M^2$, and the chirp mass $M_{\rm c} = M \eta^{3/5}$. We describe the BH spin with the parameter χ , such that $\vec{S}_{\rm BH} = m_{\rm BH}^2 \chi \hat{L}_N$. The allowed range of this parameter is $-1 \le \chi \le 1$ due to the Kerr limit and the fact that the spin could be aligned or anti-aligned with the orbital angular momentum.

Our previous study COOKL demonstrated that subtle coordinate choices can have a dramatic effect on the ambiguity function. For good coordinate choices, nearby points in parameter space should result in waveforms that appear as similar as possible to the detectors. The or-

⁶ The LIGO noise model was first described by [43] and is available as lalinspiral:XLALLIGOIPsd. The Virgo noise model is available as lalinspiral:LALVirgoPSD.

bital phase constant and the orientations of the spin and the orbital angular momenta must be specified at some reference point during the binary's evolution. Waveforms that have similar orientations and phasing where the detector is most sensitive will appear more similar to each other than waveforms that happen to coincide at some much higher or lower frequency not around peak sensitivity. For this reason, we choose $\phi_{\rm ref}$ to be the orbital phase at 100 Hz, which is approximately the peak of the SNR integrand for an inspiral-only waveform in initial LIGO.

In addition to choosing coordinates describing the loudest portion of the waveform, it is also desirable to choose coordinates for which a parameter space metric is nearly flat. There is a well-known method for metric-based placement of non-spinning inspiral templates based on the work of Owen and Sathyaprakash [47–49]. They find that the overlap (or "distance") $\mathcal{O}(h(\lambda, h(\lambda + \delta\lambda)))$ between two nearby waveforms with parameter separation $\delta\lambda$ is determined by a metric whose definition coincides with that of the Fisher matrix

$$\mathcal{O}(h(\lambda, h(\lambda + \delta\lambda))) = 1 - g_{ij}(\lambda)\delta\lambda^{i}\delta\lambda^{j}, \qquad (3)$$

$$g_{ij}(\lambda) = -\frac{1}{2}\frac{\partial^{2}\mathcal{O}}{\partial\delta\lambda^{i}\partial\delta\lambda^{j}} \simeq \left(\frac{\partial h(\lambda)}{\partial\lambda^{i}}\middle|\frac{\partial h(\lambda)}{\partial\lambda^{j}}\right) = \Gamma_{ij}.(4)$$

To lay a template bank covering the mass plane, one typically uses so-called "chirp time" parameters [47]

$$\tau_0 = \frac{5}{256} \frac{(\pi f_{\text{ref}})^{-8/3}}{M^{5/3} \eta} = \frac{5}{256} \frac{(\pi f_{\text{ref}})^{-8/3}}{\mathcal{M}_c^{5/3}}, \tag{5}$$

$$\tau_3 = \frac{\pi}{4} \frac{(\pi M f_{\text{ref}})^{-2/3}}{2\pi f_{\text{ref}} \eta} = \frac{1}{8 f_{\text{ref}} (\pi f_{\text{ref}} \mathcal{M}_c)^{2/3} \eta^{3/5}}.$$
 (6)

These are the leading and 1.5pN coefficients for the pN prediction of the time it will take an adiabatic, quasicircular inspiral to evolve from $f_{\rm ref}$ to coalescence. In this work, we use $f_{\text{ref}} = 100 \text{ Hz}$, which is the point at which we define our extrinsic parameters. The advantage of this parameterization is that the metric becomes very nearly flat in these coordinates. Since the metric is equivalent to the Fisher matrix, the Fisher matrix will be nearly constant in an appreciable region around the injected parameters, and the posterior probability distribution will be nearly Gaussian in this parameterization. We therefore re-evaluated our analytic and simulation results in several coordinate systems. We find that the posteriors have surprisingly simple form in the coordinates $(\mathcal{M}_c, 1/\eta^2, \chi)$ and give results in this parameterization as well. For the high-amplitude signal explored in this work, the posterior distribution is tightly confined: coordinate-induced nongaussianities and noiserealization-dependent parameter errors rarely occur. For

weaker signals with broader and more noise-realization-dependent posteriors, our experience suggests alternative coordinates will significantly improve the resemblence between Fisher matrix estimates and MCMC posteriors.

Recently, [50] have developed a generalized template metric approach which can be used to place spin-aligned templates. Rather than using the chirp times as coordinates, they use an 8-dimensional space of ψ_k , the pN coefficients of the stationary-phase approximation pN inspiral waveform. They then use a principal component analysis to find the dominant eigendirections (of which they only need two) in this space and lay template along those directions. In principle, it might also be interesting to display our results in a coordinate system of three or more principal eigendirections for the spin-aligned space as in [50], but finding such coordinates and relating them to the physically interesting parameters is well outside the scope and focus of this paper.

III. PARAMETER ESTIMATION METHODS

A. Bayes' theorem for GW parameter estimation

We begin this section by reviewing the basics of how Bayes' theorem can be applied to quantify how much support any stretch of gravitational wave data $\{d\}$ provides for the hypotheses H_1 , that a signal of a specific form is present, or H_0 , that the data contains only noise, and to estimate the likely parameters if a signal is present. This is largely to clarify notation and terminology, and we refer the reader to [15, 28, 51] and references therein for more information.

For sufficiently short time intervals, gravitational-wave detector data in the absence of a signal can be approximated as a Gaussian, stationary, random process characterized by a power spectrum S_h , which we take to be either of Eqs. (1-2). In the limit of a long, continuous time duration, the relation describing the noise is:

$$\langle n^*(f)n(f)\rangle = \frac{1}{2}S_h(|f|)\delta(f - f') , \qquad (7)$$

The power spectrum can also be used to define an inner product between any two signals (such as a data stream and a template waveform) for a single detector:

$$\langle a|b\rangle \equiv 2 \int_{-\infty}^{\infty} df \frac{a^*(f)b(f)}{S_h(|f|)} .$$
 (8)

Note that this defines a complex-valued inner product, while most of the gravitational-wave data analysis is written in terms of a real-valued inner product. In fact, as in COOKL, we use the complex-valued inner product for our effective Fisher matrix computations; however, our MCMC runs use a real-valued inner product acting on real-valued signals a(t), b(t), which is simply the real part of Eq. (8). All of the equations in this work involve inner products of real-valued signals with themselves, in which

⁷ For the non-precessing binaries considered here, the reference point is only relevant for the orbital phase, as the angular momenta have constant orientations.

case the real- and complex-valued inner products coincide, so we will use a common notation for either inner product. Also, while we have written the inner product as an integral over the entire real-valued frequency range, the discreteness of our signals and the low-frequency limits of our detectors mean that in practice the integration is over the frequencies $[-f_{\mathrm{Nyq}}, -f_{\mathrm{low}}] \cup [f_{\mathrm{low}}, f_{\mathrm{Nyq}}]$. By our assumptions, in the absence of a signal the noise

will follow a Gaussian distribution such that louder noise realizations (as measured by the inner-product-induced norm) are less probable according to

$$p(\lbrace d \rbrace | H_0) \propto \exp{-\frac{\langle d | d \rangle}{2}}$$
 (9)

where d(t) is the timeseries in a single detector. For a multidetector network, the posterior probability is the product of many such factors, one for each detector.

Bayes' Theorem relates the ("posterior") probability distribution $p(\lambda|\{d\}H_1)$ to the conditional probability density or likelihood, $p(\lbrace d \rbrace | \lambda, H_1)$, of the data given the signal parameters λ ; the prior probability $p(\lambda|H_1)$, describing knowledge about the parameters within the model H_1 before the data is analyzed; and the total probability of the observed data given our signal model hypothesis, $p(\lbrace d \rbrace | H_1)$:

$$p(\vec{\lambda}|\{d\}, H_1) = \frac{p(\vec{\lambda}|H_1)p(\{d\}|\vec{\lambda}, H_1)}{p(\{d\}|H_1)} , \qquad (10)$$

$$= p(\vec{\lambda}|H_1) \frac{p(\{d\}|\vec{\lambda}, H_1)/p(\{d\}|H_0)}{p(\{d\}|H_1)/p(\{d\}|H_0)} . (11)$$

In the second line we have normalized by the probability of the null hypothesis $p(\lbrace d\rbrace|H_0)$ to eliminate samplingdependent dimensional factors present in $p(\lbrace d \rbrace | H_1)$ and the likelihood $p(\lbrace d \rbrace | \lambda, H_1)$.

The user is free to quantify their prior assumptions about the parameters, $p(\lambda|H_1)$ as they see fit. We typically use uniform priors over some broad range. The actual priors used for these runs are described in the next subsection.

For each detector, we assume the data takes the form $d = h(\lambda) + n$ for some noise realization n, and we ask how likely it is to observe d. Using Eq. (9), we can compute the likelihood for a single detector [28]

$$p(\lbrace d \rbrace | \lambda, H_1) \propto \exp{-\frac{\langle d - h(\lambda) | d - h(\lambda) \rangle}{2}}$$
 (12)

and similarly for a multidetector network. In practice, with lalinference_mcmc, we work an expression which explicitly does not depend on the sampling rate or length of data being examined, the *likelihood ratio* \mathcal{L} :

$$\mathcal{L} \equiv p(\lbrace d \rbrace | \vec{\lambda}, H_1) / p(\lbrace d \rbrace | H_0)$$
 (13)

$$\mathcal{L} \equiv p(\lbrace d \rbrace | \vec{\lambda}, H_1) / p(\lbrace d \rbrace | H_0)$$

$$= \frac{e^{-\langle h(\lambda) - d | h(\lambda) - d \rangle / 2}}{e^{-\langle d | d \rangle / 2}} ,$$
(13)

where the former expression applies in general and the latter to a single detector.

To quantify our overall confidence that a signal was present, with any allowed parameter values (and to properly normalize our posterior) we compute the evidence

$$Z(d|H_1) \equiv \frac{p(\{d\}|H_1)}{p(\{d\}|H_0)} = \int d\lambda p(\vec{\lambda}|H_1) \frac{p(\{d\}|\vec{\lambda}, H_1)}{p(\{d\}|H_0)}$$
$$= \int d\lambda p(\vec{\lambda}|H_1) \mathcal{L}(\lambda|\{d\}) . \tag{15}$$

For multidetector networks, the posterior probability or likelihood of the network is simply the product of these quantities for each of the individual detectors due to the fact that probabilities interact multiplicatively.

MCMC parameter estimation: lalinference_mcmc

Several general strategies have been developed to estimate posterior distributions $p(\lambda|\{d\}, H_1)$ and evidence Z given data [52-57]. Here we use the lalinference_mcmc code to estimate the posterior parameter distribution consistent with a candidate data stream and a given noise model [15, 31]. A detailed description of the lalinference code, including its jump proposals and parallel tempering method, is far beyond the scope of this paper. In brief, the current lalinference code iteratively explores the parameter space, relying on detailed balance to construct a sequence of samples x_k for $k=1...\infty$ that converges in distribution to the true posterior distribution [52]. Though each element x_k of the chain is randomly distributed, neighboring elements are strongly correlated: the chain "wanders" through the posterior. As a result, the whole chain contains fewer effectively independent samples from the posterior than would naively be supposed from its length. To estimate the number of independent samples, we use the correlation length, defined on a parameter-by-parameter basis as the smallest nonzero s so

$$1 + \sum_{k=1}^{s} 2C(k) \le s \tag{16}$$

where $C(k) = \langle x_q x_{k+q} \rangle / \langle x^2 \rangle$ is the autocorrelation function of the sequence. In terms of this number, the effective sample size $N_{\text{eff}} \equiv N/s$ for N the chain length. As used in this work, the lalinference_mcmc code terminated when roughly $N_{\rm eff} \simeq 10^4$ independent samples

 $^{^{8}}$ In this convention, Z is more properly called an evidence ratio, odds ratio or a Bayes factor for the signal hypothesis versus the null hypothesis, rather than the standard notion of evidence $\int d\lambda p(\{d\}|\lambda H_1)p(\lambda|H_1)$. Our expression has the distinct advantage of being a dimensionless quantity, independent of the sampling rate or number of samples and fits naturally with our use of likelihood ratio.

were present in the posterior chain.⁹ We additionally required the sequences x_k of each individual parameter to satisfy standard convergence criteria (e.g., the Gelman-Rubin R statistic).

The procedure must start from some prior assumptions about the parameters, and these priors can have some influence on the details of the posterior. We assume a source could lie at any orientation and any distance within 100 Mpc, ¹⁰ uniform in volume and angle, with random masses (m_1, m_2) uniformly distributed in mass between $1M_{\odot}-30M_{\odot}$ with $m_1+m_2\leq 35M_{\odot}$ and anywhere inside a time window of length $\Delta T = 0.1$ s. When (aligned) spin is included, we allow both objects' dimensionless spins $|S_k/m_k^2|$ to lie between [0, 1] uniformly, either aligned or antialigned with the orbital angular momentum. This two-spin model space includes one more parameter than the analytic predictions in COOKL, which did not allow the smaller body to have internal angular momentum. Due to the high mass ratio, the smaller body's internal angular momentum $(|S_2| \leq m_2^2)$ is expected to have a relatively small effect on the radiated signal [58, 59].

We note that these priors are quite broad and uninformative, rather than being concentrated around the injected parameters. The prior on time of arrival (uniform in a range of length 0.1 s) may seem rather restrictive. In practice, however, parameter estimation will usually be performed after a search pipeline has claimed a likely detection; this time window is broad compared to the typical time resolution of a compact binary inspiral search pipeline.

Once the run has produced the targeted number of effectively independent samples, we can extract a number of results from the computed posterior. For example, we can find the maximum log-likelihood and the param-

⁹ This termination condition was chosen to produce reasonably-well-determined confidence intervals in each parameter. For example, to construct 90% confidence intervals requires identifying a region with only 10% probability; with N_{eff} sample points, however, the systematic accuracy in assigning a probability p to a region is of order $p/\sqrt{N_{eff}}$.

eter values at this peak. We can produce one- or twodimensional marginalized posteriors by integrating over the other parameters, and using them to find confidence intervals for various parameters. We can also use points near the maximum log-likelihood to compute approximate covariance and Fisher matrices that describe this region. All of these results can be compared between different runs and also with similar quantities produced via the effective Fisher matrix. The rest of this section describes several analytic techniques we use to facilitate such comparisons.

C. Prior volume ratio

Motivated by a locally Gaussian approximation, we define a characteristic parameter volume fraction:

$$V/V_{prior} \equiv \frac{Z(d|H_1)}{\max_{\lambda} \mathcal{L}(\lambda|\{d\})}$$
 (17)

In the limit that the posterior can be approximated by a Gaussian of the form $\mathcal{L}(\lambda)p(\lambda) \propto \exp(-\delta\lambda_a\Gamma_{ab}\delta\lambda_b/2)$ in the neighborhood of λ_* , where the local maximum's location and shape is dominated by the likelihood \mathcal{L} and not the prior p, then the prior volume ratio is simply

$$V/V_{prior} = \int d\lambda \frac{p(\lambda|H)\mathcal{L}}{\max_{\lambda} \mathcal{L}} \simeq \frac{\sqrt{|\Gamma|}}{(2\pi)^{N/2}} p(\lambda_*) ,$$
 (18)

where $|\Gamma|$ represents the determinant and N the number of parameters. Because the definition is explicitly the product of the prior times a function ≤ 1 with support concentrated in high-probability regions, the volume fraction characterizes the fraction of a priori plausible signals that are consistent with the data $\{d\}$. We can define a recovered network SNR from the max log-likelihood (ratio) as:

$$\rho_{\rm rec} \equiv \sqrt{2 \max_{\lambda} \ln \mathcal{L}(\lambda | \{d\})} \ . \tag{19}$$

To characterize how rapidly the prior volume ratio changes with $\rho_{\rm rec}$, we define a characteristic "effective dimension" as [60]

$$D_{\rm eff,rec}(\rho_{\rm rec}) \equiv -\frac{d \ln(V/V_{\rm prior})}{d \ln \rho_{\rm rec}} \ . \tag{20}$$

Intuitively, the effective dimension is the number of parameters which can be constrained relative to their prior range. For example, suppose we had a Gaussian posterior whose width in every parameter was significantly narrower than the prior. Then, the prior volume ratio would be given by Eq. (18), and we would have $D_{\rm eff}=N$. Now, suppose we added one or more parameters which have absolutely no effect on the posterior. Then, we would simply recover the prior on those parameters for any $\rho_{\rm rec}$. We would have the same $D_{\rm eff}$ as before, even though N has increased by adding unmeasurable parameters.

¹⁰ The maximum distance adopted is conventional for low-mass sources in lalinferece_mcmc. As described in Appendix C near Eq. (??), combined with the mass prior, this relatively small maximum distance allows enough rare distant and high-mass signals to significantly influence averages over the prior, including the average log likelihood. In particular, the evidence will depend on this arbitrary choice, in our opinion nonphysically. We strongly recommend subsequent calculations adopt a significantlly larger maximum distance, in significant excess of the horizon distance for all sources allowed by the mass prior, to insure comparable and astrophysically relevant evidence calculations. A detection-weighted prior on the source distance and mass prior would also regularize the distance distribution. Unfortunately, given the complexity of existing pipelines and the variability of noise, such a prior would either be interpretationdependent and ad-hoc or accurate, calculated by Monte Carlo, and variable from source to source, significantly complicating comparisons across sources.

Our non-spinning waveform model has 9 parameters and the spin-aligned model has 11. In justifying our prior range in Sec. III B, we argued that the spin of the smaller body is strongly suppressed, and so we might expect to be unable to constrain it significantly (this turns out to be the case). Furthermore, as will be discussed at length, our restricted waveforms have a degeneracy between ψ and $\phi_{\rm ref}$ such that only a certain combination of the two can be measured; amplitude-corrected waveforms break this degeneracy and allow both angles to be measured. For a sufficiently loud signal, we expect to be able to constrain all other parameters to some extent relative to their priors. Therefore, we expect the following values for $D_{\rm eff}$ for our various waveform models:¹¹

$$D_{\text{eff}}(\rho \simeq 20) = \begin{cases} 8 & \text{Zero spin, no} \\ 9 & \text{Zero spin, with} \\ 9 & \text{Aligned spin, no} \\ 10 & \text{Aligned spin, with} \end{cases}$$
(21)

where "no" indicates a model without higher harmonics and "with" a model including higher harmonics. At lower SNR, certain parameters will become poorly measured or unmeasurable, and $D_{\rm eff}$ will drop. We provide more details about the effective dimension in Appendix C. In particular, we compute $D_{\rm eff}$ via thermodynamic integration and find it's behavior changes around a network SNR $\rho_{\rm rec} \simeq 10$, indicating this is when parameter estimation begins to significantly degrade.

Both the recovered signal amplitude $\rho_{\rm rec}$ and effective dimension $D_{\rm eff,rec}$ depend on the noise realization. For example, for a fixed physical signal and random noise realizations, the recovered signal amplitude is a χ^2 -distributed random variable, with $2N_D$ degrees of freedom, where N_D is the number of detectors, normalized so $\langle \rho^2 \rangle = N_D$ in the absence of signal. To provide an invariant measure of signal strength and the local density of states, we use "noiseless" data $\{d\}_0$ where the data $d = h(\lambda_*)$ for some parameters λ_* . In particular, we define the intrinsic network amplitude $\rho(\lambda_*)$ by

$$\rho(\lambda_*) \equiv \sqrt{2 \max_{\lambda} \ln \mathcal{L}(\lambda | d = h(\lambda_*))} . \tag{22}$$

D. Comparing two distributions' shapes

On physical grounds, we want to understand how tightly individual gravitational wave measurements will constrain parameters. In particular, we want to compare the *shapes* of the nearly-Gaussian posterior probability distributions, both to each other and to analytic approximations derived using the effective Fisher matrix. Because these distributions will be approximately Gaussian, we can compare shapes using a locally Gaussian approximation. Pecifically, we compare two distributions with covariance matrices $\Sigma = K^{-1}$ and $\Sigma_* = K_*^{-1}$ by computing the quantity

$$D_{KL}(K_*, K) \equiv \frac{1}{2} \left[\ln[|K_*|/|K|] + \text{Tr}[K_*^{-1}(K - K_*)] \right] . \tag{23}$$

As described in Appendix A, this expression is a special case of a more general expression, the KL divergence, which has been extensively applied to the theory and practice of Markov Chain Monte Carlo; see [53] and references therein. In this work, we will not exploit the statistical significance of D_{KL} , treating the expression above solely as a phenomenological measure of distribution similarity. For one-dimensional distributions $K = 1/\sigma_*^2$ and $K_* = 1/\sigma_*^2$, this expression reduces to [60]:

$$D_{KL}(\sigma_*, \sigma) \equiv \ln \frac{\sigma}{\sigma_*} - \frac{1}{2} + \frac{\sigma_*^2}{2\sigma^2}$$

$$\simeq (\ln \sigma/\sigma_*)^2 + O(\ln \sigma/\sigma_*)^3$$
(24)

where in the last line we take a limit of small $\ln(\sigma/\sigma_*)$. For multidimensional distributions which share the same principal axes, $D_{KL}(K_*, K)$ separates into a sum of one-dimensional D_{KL} :

$$D_{KL}(K_*, K) = \sum_{q} D_{KL}(\sigma_{q,*}, \sigma_q)$$

More generally, however, the quantity D_{KL} in Eq. (23) severely penalizes correlations with different principal axes. As a concrete example, if K_* is a two-dimensional symmetric matrix, without loss of generality of the form

$$K_* \equiv \begin{bmatrix} \lambda_1 & 0 \\ 0 & \lambda_2 \end{bmatrix} ,$$

and $K = RK_*R^{-1}$ is a rotation of that matrix by an angle θ , then

$$D_{KL}(K_*, K) = \frac{2(\lambda_1 - \lambda_2)^2 \sin^2 \theta}{\lambda_1 \lambda_2}$$
 (25)

As a result, in the physically common case $\lambda_1 \gg \lambda_2$, a slightly misaligned error ellipsoid K with similar scales as K_* can have a large $D_{KL} \simeq 2\theta^2 \lambda_1/\lambda_2$.

Due to the computational limits of our MCMC results, each parameter x has only $N_{\text{eff}}(x)$ independent elements.

Another simple way to predict the effective dimension D_{eff} is to compute a Fisher matrix and simply count the number of eigenvalues that are smaller than the associated prior range.

¹² In more general cases with less-Gaussian posteriors, similarity between two one-dimensional posteriors is often quantified via a Kolmogorov-Smirnov (KS) test. We adopt the KL-divergence method due to its more attractive scaling with dimension and its clear treatment of differing correlations.

Our best estimate for the sample standard deviation, $\hat{\sigma}^2 = \sum_k (x - \bar{x})^2 / (N - 1)$, has sampling error. Assuming a Gaussian distribution, this estimator has a relative mean-squared error¹³

$$\frac{\left\langle (\hat{\sigma}^2 - \left\langle \hat{\sigma}^2 \right\rangle)^2 \right\rangle^{1/4}}{\sigma} \simeq \frac{2^{1/4}}{(N-1)^{1/4}} \,. \tag{26}$$

In particular, the standard deviation calculated from a relatively small number of effective samples $N_{\rm eff} \simeq 10^3-10^4$ can vary noticeably between different Markov chains, by tens of percent at least. These statistical fluctuations from different MCMC realizations produce errors that add in quadrature with the statistical fluctuations associated with different noise realizations, described below. These statistical fluctuations limit our ability to distinguish between two distributions with too-similar widths $(\ln \sigma/\sigma_* \lesssim 1/\sqrt{N})$ and hence too-small D_{KL} $(D_{KL} \lesssim 1/N)$.

Motivated by more detailed discussions (see, e.g., Eqs. (33-36) in O'Shaughnessy [60] and Appendix A), we anticipate that we choose between two hypotheses H_1 (a gaussian with covariance K) and H_2 (a gaussian with covariance K_*) with $N_{\rm eff}$ samples if the two Gaussian distributions have KL divergence above an $N_{\rm eff}$ -dependent threshold:

$$D_{KL} \gtrsim \frac{10}{N_{\text{eff}}} \times d$$
 (27)

where the d in the numerator is the number of dimensions in K. The factor 10 was chosen via a Monte Carlo over two one-dimensional gaussian distributions, to reduce the false alarm probability to less than 10^{-4} . Similarly, two samples will have distinguishable width if $D_{KL}(\sigma_1, \sigma_2)$ is greater than roughly twice this threshold.

Though fully accounting for finite-MCMC-length effects, the above condition does not account for detector noise. If we construct the posterior for a special data realization – exactly zero noise – the best-fit parameters will be the physical parameters λ_* and the posterior will have a locally Gaussian shape set by K_* . Each noise realization shifts the best-fit point and changes the associated posterior's shape. In the Gaussian limit, the best-fit parameters λ are consistent with a Gaussian defined by K_* , centered on the physical parameters; the best-fit signal amplitude $\hat{\rho}$ differs from the physical signal amplitude ρ

by a random number of order unity; and the posterior covariance K therefore differs from K_* by two effects: change in ρ and K. In the first case, because the posterior scales as $K \propto \rho^2$ (i.e., $\sigma \propto 1/\rho$), fluctuations in the signal amplitude directly produce fluctuations in σ and K. In the large- ρ limit, we anticipate and Monte Carlo simulations confirm that the D_{KL} between the intrinsic and sample-estimated K will fluctuate. Substituting in two proportional d-dimensional covariance matrices $K_*\rho_*^2$ and $K_*\rho^2$ into Eq. (23), we find that fluctuations in the scale factor (ρ) have relatively little effect:

$$D_{KL}(K_*\rho_*^2, K_*\rho^2) = -\frac{1}{2}\ln(\rho/\rho_*)^{2d} + \frac{d}{2}((\rho/\rho_*)^2 - 1)$$
$$\simeq d\left(\frac{\delta\rho}{\rho_*}\right)^2 \tag{28}$$

Each of the N_D detectors contributes a comparable noise in the signal amplitude, so $\delta\rho$ is χ^2 distributed with $\langle\delta\rho^2\rangle=N_D$. As a result, random fluctuations due to the noise realization produce unavoidable changes in the posterior's shape relative to the noiseless posterior, characterized by a typical D_{KL} of order

$$\langle D_{KL}(K_*\rho_*^2, K_*\rho^2) \rangle \simeq dN_D/\rho^2$$

 $\simeq 0.0675(N_D/3)(d/9)(\rho/20)^{-2}$
(29)

Any value of D_{KL} comparable to or smaller than this expression suggests the two distributions have effectively indistinguishable shapes. This uncertainty adds (linearly) to the error expected from finite $N_{\rm eff}$; for $N_{\rm eff} \gtrsim 10^3$, this expression is the dominant source of error.

Conversely, to be confident two distributions have dif-ferent shapes, we want D_{KL} between those two covariances to be several standard deviations away. Again using a one-dimensional Gaussian Monte Carlo to select the prefactor, we consider two distributions to be clearly distinguishable if

$$D_{KL}(K_*, K) \gtrsim \frac{4N_D}{\rho^2} \times d \tag{30}$$

where the coefficient insures a probability less than 10^{-4} . Finally, our approach to diagnosing posterior differences is both qualitatively and quantitatively useful only when the posterior is locally Gaussian. A gaussian with covariance K^{-1} is only a good approximation in a small region. Roughly speaking, when error ellipsoids approximated by K are sufficiently long and narrow, the locally Gaussian approximation can break down, simply because the covariance K^{-1} changes from point to point. In the worst case, ubiquitous in the limit of low signal amplitude, the error "ellipsoids" are not ellipsoidal. Less catastrophically, the principal axes and eigenvalues of K can vary rapidly over the signal space; as a result, when the best-fit parameters λ are far from the physical values, the posterior's covariance K will differ significantly from the predicted (zero-noise) limit. This second challenge

 $^{^{13}}$ Briefly, on physical grounds, measurements can at best distinguish one "natural" parameter to a relative accuracy $1/\sqrt{N}.$ Because the standard deviation naturally enters quadratically into the distribution and hence into all derived expressions, it can be measured to a relative accuracy $1/n^{1/4}.$ Conversely, the dramatic variation in σ between data realizations and the slow convergence of those fluctuations with N is a feature of the coordinates used to characterize the posterior. As alternative coordinates make clear, evidence favoring one Gaussian distribution over another accumulates linearly with the number of samples N

can be mitigated or completely eliminated by adopting a different coordinate system to parameterize the binary. For the systems explored in this work, a local gaussian approximation is effective, so alternative coordinate systems only marginally improve our already good agree-

Strong nongaussianities can also arise from edge effects which restrict a posterior to be defined to a narrow range. We do not modify our procedure to account for edge effects, e.g. from the upper bound on the mass ratio or black hole spin.

Quantifying multidimensional correlations

COOKL suggested that the posterior for nonprecessing binaries largely separates into purely intrinsic and purely extrinsic parameters, even in the presence of higher harmonics, when the posterior is marginalized over polarization and event time. If true, this powerful constraint implies posteriors can be understood using far fewer correlations.

Motivated by information theory, we quantify the degree of correlation between two subspaces A, B using the mutual information [51]. For the case of a multidimensional Gaussian with subspaces A and B, the mutual information of the two subspaces is

$$I(A,B) \equiv \frac{1}{2} \ln \frac{|\Sigma_A||\Sigma_B|}{|\Sigma|} ,$$
 (31)

where Σ_A and Σ_B are projections of the full covariance matrix Σ onto the A, B subspaces, respectively. This expression provides a way to evaluate the degree of correlation between two parameter subspaces that does not change under local linear transformation.

To illustrate how this measure of similarity compares with another often-used measure, the correlation coefficient, we apply Eq. (31) to a two-dimensional covariance matrix of the form

$$\Sigma = \begin{bmatrix} \sigma_A^2 & \sigma_A \sigma_B c_{AB} \\ \sigma_A \sigma_B c_{AB} & \sigma_B^2 \end{bmatrix}$$
(32)
$$I(A, B) = \frac{1}{2} \ln \frac{1}{1 - c_{AB}^2} .$$
(33)

$$I(A,B) = \frac{1}{2} \ln \frac{1}{1 - c_{AB}^2} . \tag{33}$$

It is clear that I(A, B) will be zero if A and B are completely uncorrelated, and larger values indicate a greater degree of correlation. The mutual information is unbounded and diverges in the case where A and B are perfectly correlated or anti-correlated.

Using a finite number of samples produces errors in Σ and hence in I. For our purposes, the information I will indicate an identifiable correlation if

$$I \gtrsim \frac{10[\dim(A) + \dim(B)]}{N_{\text{eff}}}$$
 (34)

This rule of thumb was found empirically by performing a Monte Carlo with a simple two-dimensional toy model, finding a cutoff which ensures two uncorrelated subspaces are claimed as correlated with a false alarm probability of 10^{-4} , and scaling properly with N_{eff} , dim(A) and $\dim(B)$.

Bounded parameters and truncated distributions

In the above discussion of numerical and analytic posteriors, we have implicitly assumed all parameter combinations are allowed. In fact, many parameters are defined over a bounded nonperiodic domain, such as $\eta \in [0, 1/4]$, and $|\chi| \leq 1$ (but not $\phi \in [0, 2\pi]$). In the limit of high signal amplitude, the posterior will resemble a truncated Gaussian $p(x)\theta_D(x)$ where $\theta_D(x)$ is a suitable step function to limit x to the allowed parameter region D and p(x) is a Gaussian over the parameters x. Many of our posterior distributions have this property. For example, because we specify an extremal black hole spin $\chi = 1$, our posterior distributions cannot be Gaussian into the regime $\chi > 1$.

Even though the D_{KL} expression was derived using Gaussian distributions, it provides an equally well-posed scheme to compare any two covariances Σ, Σ_* . We therefore apply it unchanged when comparing any pair of predictions, such as for distributions that are truncated due to bounded parameters.

Truncation becomes more of an issue when comparing the predicted posterior distributions involving spin. Because the signal is highly degenerate, limits on χ constrain the extent of the three-dimensional distribution in $\mathcal{M}_c, \eta, \chi$. By contrast, Fisher matrix calculations of the kind described in COOKL do not include this prior. As a result, due to truncation, even if the Gaussian p(x) in $p(x)\theta_D(x)$ and the Fisher matrix prediction are identical, because the covariance of the distribution $p(x)\theta_D$ differs from the covariance of p(x), truncation introduces additional systematic differences between the effective Fisher matrix approximation and the results of detailed calculations.

We note that for our fiducial binaries $\eta = 0.1077$ is right in the middle of its domain, well away from the boundaries. As such, the bounds on η do not affect our results. However, if we were to study, for example, an equal mass binary then the η distribution would be truncated much like the spin distribution is in this case.

IV. PARAMETER ESTIMATION RESULTS

For our fiducial binaries, one with and one without BH spin, we generate target inspiral signals with and without higher harmonics, using a specific sky location and event time; see Tables I and II for details. Each signal is injected into random Gaussian noise, then systematically compared with a source model from the same waveform family (SpinTaylorT4) including identical physics:

| Source | Harmonics | Seed | $ ho_{ m inj}$ | $ ho_{ m rec}$ | $\ln Z$ | $\ln V/V_{prior}$ | $N_{ m eff}$ |
|--------------|-----------|--------|----------------|----------------|---------|-------------------|--------------|
| Zero spin | no | - | 20.33 | 20.64 | 180. | -33.4 | 7517 |
| Zero spin | no | _* | 20.33 | 20.64 | 179. | -34.2 | 9347 |
| Zero spin | no | 1234 | 20.33 | 20.5 | 176. | -34.2 | 10697 |
| Zero spin | no | 1234* | 20.33 | 19.42 | 156. | -32.5 | 7501 |
| Zero spin | no | 56789 | 20.33 | 20.34 | 172. | -34.8 | 10403 |
| Zero spin | no | 56789* | 20.33 | 21.65 | 207. | -27.3 | 10000 |
| Zero spin | with | - | 21.03 | 21.33 | 191. | -36.3 | 8027 |
| Zero spin | with | _* | 21.03 | 21.34 | 191. | -36.9 | 7348 |
| Zero spin | with | 1234 | 21.03 | 21.76 | 200. | -37. | 7511 |
| Zero spin | with | 1234* | 21.03 | 20.38 | 170. | -36.9 | 6523 |
| Zero spin | with | 56789 | 21.03 | 20.67 | 177. | -36.6 | 11358 |
| Zero spin | with | 56789* | 21.03 | 22.12 | 204. | -40.4 | 22843 |
| Aligned spin | no | - | 22.34 | 22.67 | 222. | -34.6 | 9841 |
| Aligned spin | no | _* | 22.34 | 22.66 | 223. | -34.2 | 10174 |
| Aligned spin | no | 1234 | 22.34 | 22.81 | 225. | -35.1 | 8670 |
| Aligned spin | no | 1234* | 22.34 | 21.90 | 206. | -32.8 | 126040 |
| Aligned spin | no | 56789 | 22.34 | 24.89 | 272. | -37.5 | 10508 |
| Aligned spin | no | 56789* | 22.34 | 22.62 | 220. | -35.5 | 10003 |
| Aligned spin | with | - | 22.88 | 23.19 | 230. | -38.9 | 4289 |
| Aligned spin | with | _* | 22.88 | 23.20 | 232. | -37. | 1737 |
| Aligned spin | with | 1234 | 22.88 | 23.67 | 240. | -40.1 | 8569 |
| Aligned spin | with | 1234* | 22.88 | 22.65 | 217. | -38.9 | 10866 |
| Aligned spin | with | 56789 | 22.88 | 25.4 | 279. | -43.3 | 10715 |
| Aligned spin | with | 56789* | 22.88 | 23.37 | 237. | -34.9 | 34921 |

TABLE III: Simulation results: Table of distinct simulations performed. The first set of columns indicate which of the two fiducial binaries was used (zero spin vs aligned spin), whether higher harmonics were included (up to 1.5PN in amplitude), and random seed choice used to generate noise (a "-" means no noise was used; the asterisk indicates a different noise realization, MCMC realization, and initial orbital frequency). The two quantities $\rho_{\rm inj}$, $\rho_{\rm rec}$ provide the injected and best-fit total signal amplitude in the network [Eqs. (19,22)]. The latter quantity depends on the noise realization of the network. [For zero noise and given infinitesimal time and frequency resolution, the injected and recovered amplitudes should agree. Due to finite resolution, a different (continuously-timeshifted) template can slightly better fit a discretely-sampled signal, leading to $\rho_{rec} - \rho_{inj} > 0$.

The columns for $\ln Z$ and $V/V_{\rm prior}$ provide the evidence [Eq. (15)] and volume fraction [Eq. (17)]; the evidence, volume fraction, and signal amplitude are related by $\rho_{\rm rec}^2/2 = \ln Z/(V/V_{\rm prior})$. For each binary, two indepedent MCMC posteriors were constructed with zero noise ("-" and "-*"); the nonzero difference between their $\ln Z$ and their $\ln(V/V_{\rm prior})$ suggests how robust our estimates of these quantities are, as described at length in Appendix A. Finally, $N_{\rm eff}$ is the effective number of independent samples in our calculations.

higher harmonics if and only if the signal included higher harmonics; spin if and only if the BH had nonzero spin. Table III lists the specific simulations performed, providing the injected and recovered signal-to-noise ratio. For each simulation, Table IV provides the marginalized onedimensional uncertainties in all parameters except source inclination and distance. Finally, Table V uses D_{KL} to compare the simulations' intrinsic posterior distributions for $(\mathcal{M}_c, \eta, \chi)$ to one another and to our analytic estimates. In Figs. 1-4, we use selected two-dimensional posterior distributions derived from "zero noise" data to illustrate our principal conclusions. First, for the same binary, we consistently predict similarly-shaped distributions for intrinsic parameters $(\mathcal{M}_c, \eta, \chi)$. For most simulations, differences between the posteriors are qualitatively consistent with random chance, limited by signal

amplitude fluctuations (e.g., noise-realization-dependent differences in recovered ρ). As a concrete example, we have performed multiple zero-noise, zero-spin simulations and found differences consistent with our expectations [e.g., as suggested by Eq. (27)]. Second, using apples-to-apples comparisons of the same binary in the same noise, we consistently find higher harmonics provide minimal additional information about intrinsic parameters. Instead, higher harmonics provide geometric information. Finally, we confirm that for aligned-spin binaries, the intrinsic and extrinsic parameters nearly separate when marginalized over event time.

| Source | Harmonics | Seed | $\sigma_{\mathcal{M}_c}$ | σ_{η} | σ_χ | σ_{ψ_+} | σ_{ψ} | σ_t | σ_{RA} | σ_{DEC} | σ_A |
|--------------|-----------|--------|--------------------------|-----------------|---------------|-------------------|-----------------|------------|---------------|----------------|------------|
| | | | $\times 10^3$ | $\times 10^3$ | | · | | ms | \deg | \deg | \deg^2 |
| Zero spin | no | - | 2.13 | 1.40 | - | 0.095 | 1.8 | 0.32 | 0.48 | 0.73 | 1.0 |
| Zero spin | no | -* | 2.15 | 1.39 | - | 0.095 | 1.8 | 0.31 | 0.49 | 0.74 | 1.1 |
| Zero spin | no | 1234 | 2.26 | 1.40 | - | 0.098 | 1.8 | 0.28 | 0.48 | 0.69 | 0.96 |
| Zero spin | no | 1234* | 2.35 | 1.57 | - | 0.10 | 1.8 | 0.36 | 0.6 | 0.9 | 1.4 |
| Zero spin | no | 56789 | 2.57 | 1.52 | - | 0.1 | 1.8 | 0.32 | 0.53 | 0.76 | 1.2 |
| Zero spin | no | 56789* | 2.11 | 1.43 | - | 0.1 | 1.7 | 0.43 | 2.9 | 1.3 | 6.8 |
| Zero spin | with | - | 1.97 | 1.25 | - | 0.091 | 0.67 | 0.26 | 0.42 | 0.67 | 0.81 |
| Zero spin | with | _* | 1.94 | 1.24 | - | 0.09 | 0.67 | 0.26 | 0.42 | 0.65 | 0.79 |
| Zero spin | with | 1234 | 1.90 | 1.16 | - | 0.088 | 0.67 | 0.23 | 0.4 | 0.63 | 0.70 |
| Zero spin | with | 1234* | 2.12 | 1.35 | - | 0.099 | 0.55 | 0.28 | 0.49 | 0.75 | 0.98 |
| Zero spin | with | 56789 | 2.34 | 1.33 | - | 0.095 | 0.75 | 0.24 | 0.43 | 0.69 | 0.87 |
| Zero spin | with | 56789* | 2.04 | 1.40 | - | 0.099 | 0.45 | 0.32 | 0.53 | 0.66 | 1.1 |
| Aligned spin | no | - | 6.19 | 7.89 | 0.038 | 0.088 | 1.8 | 0.37 | 0.41 | 0.63 | 0.71 |
| Aligned spin | no | _* | 6.33 | 8.28 | 0.039 | 0.087 | 1.8 | 0.4 | 0.4 | 0.62 | 0.70 |
| Aligned spin | no | 1234 | 5.50 | 7.12 | 0.029 | 0.088 | 1.8 | 0.39 | 0.49 | 0.67 | 0.82 |
| Aligned spin | no | 1234* | 6.04 | 7.00 | 0.033 | 0.087 | 1.6 | 0.28 | 0.43 | 0.72 | 0.85 |
| Aligned spin | no | 56789 | 4.70 | 4.34 | 0.021 | 0.077 | 1.8 | 0.26 | 0.37 | 0.57 | 0.59 |
| Aligned spin | no | 56789* | 6.83 | 8.54 | 0.050 | 0.095 | 1.8 | 0.3 | 0.4 | 0.62 | 0.68 |
| Aligned spin | with | - | 5.26 | 5.94 | 0.035 | 0.087 | 0.63 | 0.24 | 0.33 | 0.55 | 0.50 |
| Aligned spin | with | _* | 5.38 | 6.19 | 0.035 | 0.087 | 0.63 | 0.25 | 0.34 | 0.55 | 0.51 |
| Aligned spin | with | 1234 | 4.73 | 5.05 | 0.030 | 0.082 | 0.62 | 0.21 | 0.36 | 0.59 | 0.55 |
| Aligned spin | with | 1234* | 4.84 | 4.87 | 0.027 | 0.089 | 0.64 | 0.21 | 0.32 | 0.56 | 0.47 |
| Aligned spin | with | 56789 | 3.91 | 4.12 | 0.016 | 0.072 | 0.38 | 0.3 | 0.42 | 0.54 | 0.71 |
| Aligned spin | with | 56789* | 7.23 | 10.0 | 0.056 | 0.095 | 0.92 | 0.43 | 0.39 | 0.6 | 0.64 |
| | | | | | | | | | | | |

TABLE IV: One-dimensional parameter errors: Measurement accuracy σ_x for x, one of several intrinsic $(\mathcal{M}_c, \eta, \chi)$ and extrinsic (ψ_{\pm}, t, RA, DEC) parameters. The extrinsic parameters are the polarization and orbital phase combinations $\psi_{\pm} \equiv \psi \pm \phi_{\rm ref}$ defined on $[-\pi/2, \pi/2]$, so $\sigma_{\psi} = 1.81$ is consistent with a uniform distribution; the event time t; the sky position measured in RA and DEC; and the sky area A, estimated using the 2×2 covariance matrix Σ_{ab} on the sky via $\pi|\Sigma|$. One simulation recovers nonzero probability at two antipodal sky locations, significantly increasing Σ above the "natural" value associated with each best-fit peak; impacted parameters are shown in boldface. For selected cases, these measurement accuracies are demonstrated in Figure 4. Comparing simulations with identical noise realizations with and without higher harmonics, this table suggests higher harmonics have minimal impact on most parameters, except for ψ_- . Comparing simulations with identical physics but different noise realizations suggests that even for our optimistic signal amplitude, the information provided by higher harmonics is small, comparable to fluctuations due to the noise realization. All parameter accuracies shown qualitatively agree with simple numerical estimates derived from the Fisher matrix or timing [Section V C], up to tens of percent relative fluctuations due to finite sample size [Eq. (26)].

A. Intrinsic distributions agree

As illustrated strikingly by Figure 1, our zero-spin simulations consistently produce tightly-confined, highly-Gaussian, similarly-shaped posteriors in \mathcal{M}_c , η . Small but nonzero differences in shape, size and position do exist between different noise realizations. Quantitatively, however, these shape differences have comparable magnitude to the effects expected when comparing different noise fluctuations, as seen by the corresponding column in Table III.

Similarly, even for the 99.9% confidence intervals in the left panel of Figure 2, our aligned-spin simulations roughly agree. Over this relatively large region of parameter space, particularly in mass ratio, the posterior distribution is not Gaussian in \mathcal{M}_c , η , χ coordinates at this confidence level. Even in these coordinates, however, as illustrated using the 90% confidence intervals in Figure 3, most of the probability is adequately approximated by some locally-Gaussian approximation, times a cutoff at $\chi = 1$. Strictly speaking, this cutoff forces the local distribution to be locally non-Gaussian and forces the local covariance to be both noise-realization-dependent and different from our analytic calculations. In practice, ignoring these subtleties and treating the posterior as locally Gaussian, however, we find all posteriors have surprisingly similar one-, two-, and three-dimensional covariances Σ , as quantified in Table IV.

Figure 2 also illustrates the value of well-chosen coordinates. As seen in the left panel of Figure 2, using

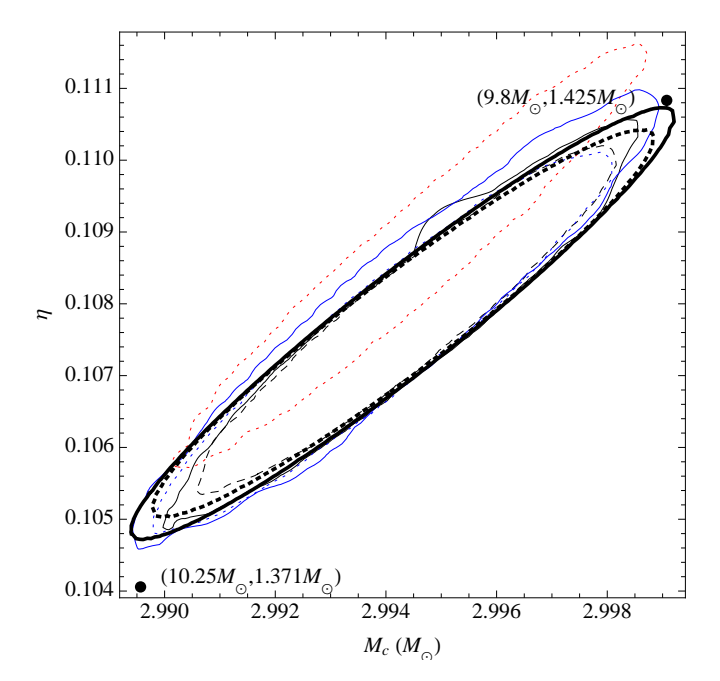


FIG. 1: Chirp mass and mass ratio 90% confidence interval: Zero spin: Assuming our fiducial nonspinning signal is present in distinct realizations of Gaussian noise (colors, described below), the contour shows the 90% confidence intervals for \mathcal{M}_c , η derived from the half of our zero-spin calculations marked with "*". Solid curves correspond to a signal without higher harmonics; dashed curves include higher harmonics; and colors denote specific noise realizations listed in Table III, not all of which appear in this figure: zero noise (black); 1234 (blue); and 56789 (red). [To better distinguish between cases including higher harmonics, the zero noise case is shown as a black dashed curve. All posteriors have similar shape; differences between the estimated posteriors are consistent with finite sample and noise realization effects. Higher harmonics do not improve our estimates of intrinsic parameters in any noticeable way. For comparison, the thick black solid and dotted curves are analytic estimates using the effective Fisher matrix normalized to $\rho = 20$, described in greater detail in Section V. To help translate these results to an astrophysically relevant scale, the two black points and pairs indicate the chirp mass and mass ratios corresponding to $(m_1/M_{\odot}, m_2/M_{\odot})$.

 $(\mathcal{M}_c, \eta, \chi)$ coordinates the error contours are both weakly nonellipsoidal and have shape that weakly depends on noise realization. As seen in the right panel of Figure 3, however, alternative coordinates mitigate nongaussianity and reduce noise-realization-dependent effects. This improvement persists for low signal amplitudes, which have broader posteriors than shown here.

B. Marginal information from higher harmonics is confined to source orientation

Using apples-to-apples comparisons of the same source in the same data, we can explicitly confirm that higher harmonics provide minimal new information about intrinsic parameters. In fact, the differences between the zero-spin, zero-noise posterior in \mathcal{M}_c , η calculated with and without harmonics are at best comparable to the fluctuations seen between different data realizations; see Table IV for the one-dimensional measurement errors, Table V for comparisons between simulations using D_{KL} , and Table III for a comparison using V/V_{prior} .

With aligned spin, higher harmonics seem to provide some additional information. For example, Figure 3 shows the two-dimensional posteriors in \mathcal{M}_c , η for three starred data realizations (black, red, blue) both with (dotted) and without (solid) higher harmonics; each pair of contours differ slightly in direction and extent. These distributions are manifestly similar: the presence of higher have less of an effect than a change of noise realization (e.g., a change in ρ of order unity). Physically, though higher harmonics provide information, different data realizations shift the error ellipsoids' positions, orientations, and scales so much that their marginal impact cannot be easily isolated. In all cases, however, higher harmonics seem to provide minimal additional information about our two fiducial sources' intrinsic parameters.

By contrast, as illustrated by Figure 4, higher harmonics do provide geometric information, improving our knowledge about the source position and orientation relative to the line of sight. Higher harmonics are known to break almost-perfect degeneracies present in the leading-order gravitational wave signal [33–35]. This signal can be represented in a compact complex form as

$$h = h_{+} - ih_{\times} = -e^{-2i\psi} \frac{8\mu v^{2}}{d_{L}} \sqrt{\frac{\pi}{5}}$$

$$\times \left[e^{-2i\Phi_{orb}} Y_{22}^{(-2)}(\iota, 0) + e^{2i\Phi_{orb}} Y_{2-2}^{(-2)}(\iota, 0) \right]$$
(35)

where $Y_{lm}^{(s)}$ are spin-weighted spherical harmonics and we note that 14 :

$$Y_{22}^{(-2)}(\iota,0) = \frac{1}{2}\sqrt{\frac{5}{\pi}}\cos^4\left(\frac{\iota}{2}\right) = \frac{1}{8}\sqrt{\frac{5}{\pi}}\left(1 + \cos\iota\right)^2(36)$$

$$Y_{2-2}^{(-2)}(\iota,0) = \frac{1}{2}\sqrt{\frac{5}{\pi}}\sin^4\left(\frac{\iota}{2}\right) = \frac{1}{8}\sqrt{\frac{5}{\pi}}\left(1 - \cos\iota\right)^2(37)$$

For most orientations, either one or the other spinweighted harmonic dominates this sum¹⁵. Our two sources have $\iota = \pi/4$, so the (2,2) mode dominates by a factor $\cos^4(\pi/8)/\sin^4(\pi/8) \simeq 34$. This means that to a good approximation the gravitational wave signal depends on ψ and $\phi_{\rm ref}$ principally through $\psi + \phi_{\rm ref}$ and on d_L and ι through $(1 + \cos \iota)^2/d_L$. More generally, in the absence of higher harmonics, to a first approximation the

¹⁴ The azimuthal argument of $Y_{22}^{(-2)}$ is degenerate with $\phi_{\rm ref}$, so we can set it to zero without loss of generality.

 $^{^{15}}$ Only when the binary is nearly edge-on, i.e. $\iota \simeq \pi/2,$ are the two comparable

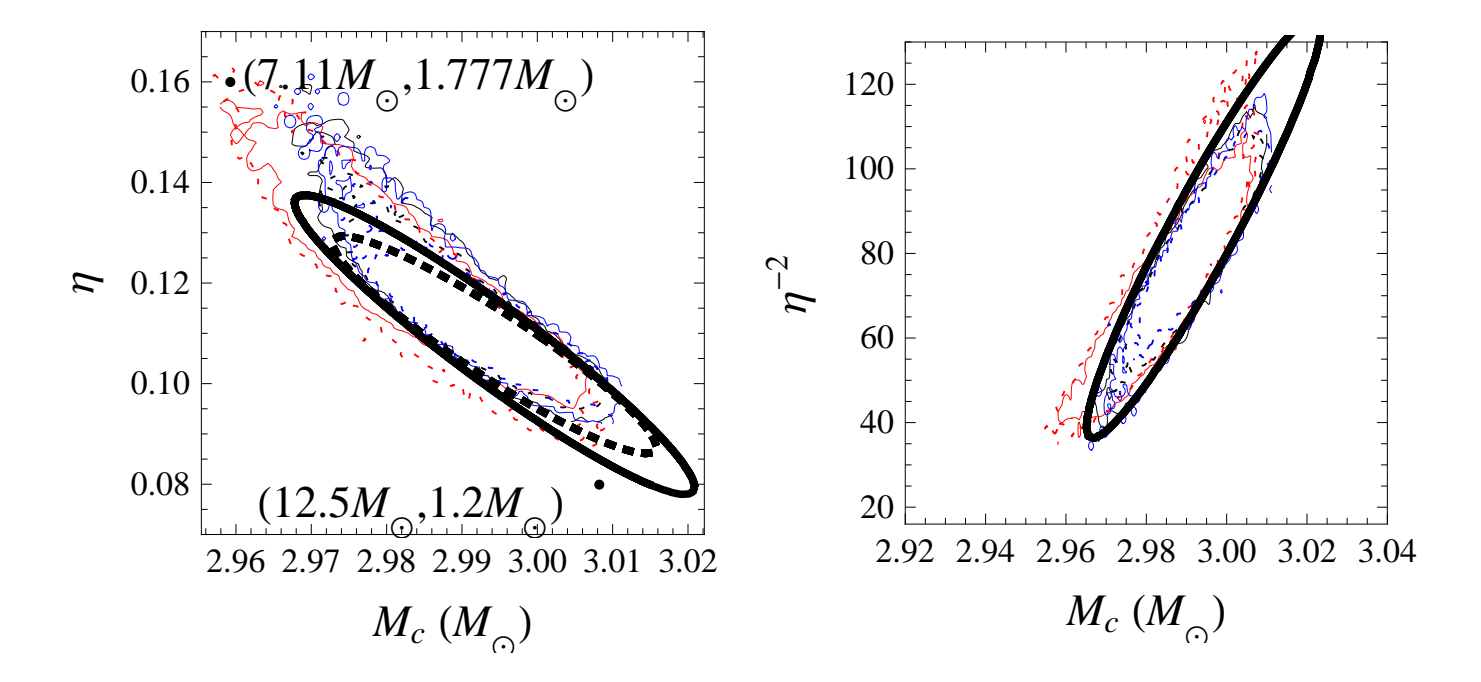


FIG. 2: 99.9% confidence intervals in mass plane for aligned-spin binary: For our fiducial aligned-spin signal injected into distinct realizations of Gaussian noise (colors, as described in the caption to Figure 1), the contours show the 99.9% confidence intervals from each calculation in our various coordinates for the mass plane. Contour styles are as described in Figure 1. This figure conveys three key points. First, the similarity between the blue solid and dotted contours shows higher harmonics provide little additional information about intrinsic parameters. Second, measurements of spinning binaries can at best weakly distinguish the individual masses in BH-NS binaries. For comparison, the solid points and associated (m_1, m_2) pairs show where those points lie in the \mathcal{M}_c , eta plane. For our loud fiducial signal, the NS mass is constrained to lie well within the range allowed from prior expereince. Third, suitable coordinates can simplify all posterior probability distributions, independent of noise realization.

distance, inclination, polarization, and orbital phase enter into the signal via $e^{-2i(\psi \pm \phi_{\rm ref})}(1 \pm \cos \iota)^2/d_L$. This functional form explains the two-dimensional correlations between $(\psi, \phi_{\rm ref})$ and (ι, d_L) shown in Figure 4.

When higher harmonics are included in the signal, the expression for h in Eq. (35) generalizes to a sum over many multipoles $h_{lm}Y_{lm}^{(-2)}(\iota,0)$, each with a distinct angular dependence. Unlike the leading-order case, several terms contribute to the overall amplitude for our fiducial case $\iota = \pi/4$ (and in general), with each harmonic having a different dependence on ι and $\phi_{\rm ref}$. As a result, a signal including higher harmonics communicates additional information about its orientation, as illustrated by the dotted curves in Figure 4. As with intrinsic parameters, however, the amount of information we gain about source orientation seems to depend on the specific noise realization.

C. Bounding the relative impact of higher harmonics

Including gravitational wave content beyond the leading-order quadrupole provides greater signal power

and hence on average provides stronger constraints on source physics. Using selected low-dimensional examples, we have used the correlation matrix Σ to suggest that higher harmonics provide relatively little new information about source physics. In this section, we argue that our information census has already identified all ways that higher harmonics can improve our understanding of this source.

To define the relative impact of higher harmonics invariantly, we use V/V_{prior} as computed via Eq. (17). This quantity is a ratio of characteristic (parameter) volumes: the volume consistent with observations and the prior volume. It is straightforward to calculate from our simulations and does not require any assumptions such as approximate Gaussianity. By comparing measurements with and without higher harmonics, we can quantify their

¹⁶ For sufficiently strong sources, we could assume the Fisher matrix provides a valid approximation to the posterior and compute the prior volume ratio from its determinant, as in Eq. (18). However, we do not rely on this assumption and instead compute it directly from the evidence.

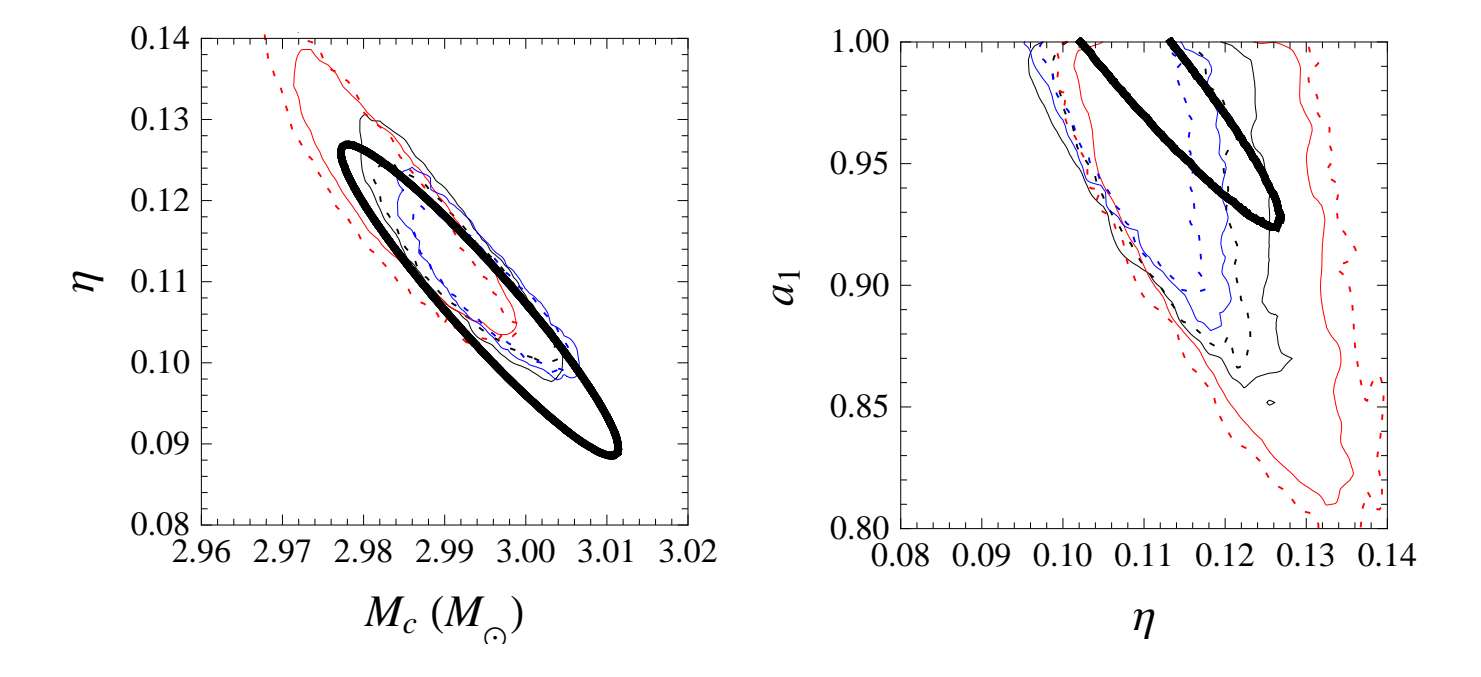


FIG. 3: 90% confidence intervals for aligned-spin binary: For our fiducial aligned-spin signal injected into distinct realizations of Gaussian noise (colors, as described in the caption to Figure 1), the contour shows the 90% confidence intervals from each calculation in the \mathcal{M}_c , η plane (left panel) and the η , χ plane (right panel). Contour styles are as described in Figure 1; as previously, the heavy black solid and dashed curves show revised analytic predictions using the COOKL method, provided in Table VII.

relative impact. The results of these comparison are summarized in Tables III and IV.

To provide a sense of scale, the numerical increase in evidence and decrease in $V/V_{\rm prior}$ can be estimated using the signal amplitude ρ and the expected number of measurable dimensions $D_{\rm eff}$. A model with higher harmonics has a higher signal amplitude ρ in any noise realization; for the nonspinning model with zero noise and hence 8 or 9 parameters, ρ is 21.03 versus 20.32, respectively [Table III]. The evidence scales as $Z \propto \rho^{-D_{\rm eff}} \exp(\rho^2/2)$ [Eqs. (20,17,19)]; for example, $\Delta \ln Z \simeq 7.5$ between the nonspinning model with and without higher harmonics, in zero noise. This expression crudely explains the large evidence differences between scenarios with and without higher harmonics, up to systematic errors in our calculation of $\ln Z$ explained in Appendix C. Similarly, the prior volume scales as

$$\Delta \ln(V/V_{\rm prior}) \simeq -D_{\rm eff} \Delta \ln \rho \simeq -D_{\rm eff} \Delta \rho/\rho$$
 (38)

This expression suggests that the volume fraction $V/V_{\rm prior}$ deceases relatively little because the amplitude increases little; for example, this expression suggests $\Delta \ln(V/V_{\rm prior}) \simeq 0.3$ for the zero-spin binary in zero noise. In fact, higher harmonics have a much more significant effect on $V/V_{\rm prior}$ than this estimate would suggest: $\Delta \ln(V/V_{\rm prior}) \simeq -3$ (zero spin) or perhaps -4 (aligned spin). Higher harmonics provide more information than

the increase in SNR would suggest by breaking degeneracies in the Fisher matrix. For this system, though, our experience with most one- and two-dimensional distributions [Table IV and Figures 1, 3, and 4] suggests the broken degeneracy is between two largely uninteresting parameters (the polarization angle ψ and the reference orbital phase $\phi_{\rm ref}$) with small improvements in measurability distributed among the other parameters.

Because $\ln(V/V_{prior})$ changes by less than 3 in our simulations, higher harmonics cannot improve the product of uncertainty in parameters by more than a factor $e^{-3} \simeq 20$. By contrast, for the systems simulated, higher harmonics improve our ability to measure one polarization combination (here, ψ_-), reducing σ_{ψ_-} by about a factor of 3 [Table IV] – roughly 1/3 of all of the available information content. The remaining factor is distributed among small changes in the remaining 8 parameter combinations, at the tens of percent level or less (i.e., set by $(\ln 20/3)/d$). These results strongly suggest higher harmonics have little global impact, bounding above the extent to which higher harmonics can modify global correlations for these strong nonprecessing signals.

Similar conclusions can be drawn from almost all of our simulations with noise: comparing simulations with the same noise realization and physics with and without higher harmonics, usually $\ln(V/V_{\rm prior})$ changes by less than of order 3. That said, a few pairs of simulations have claimed prior volume differences that are

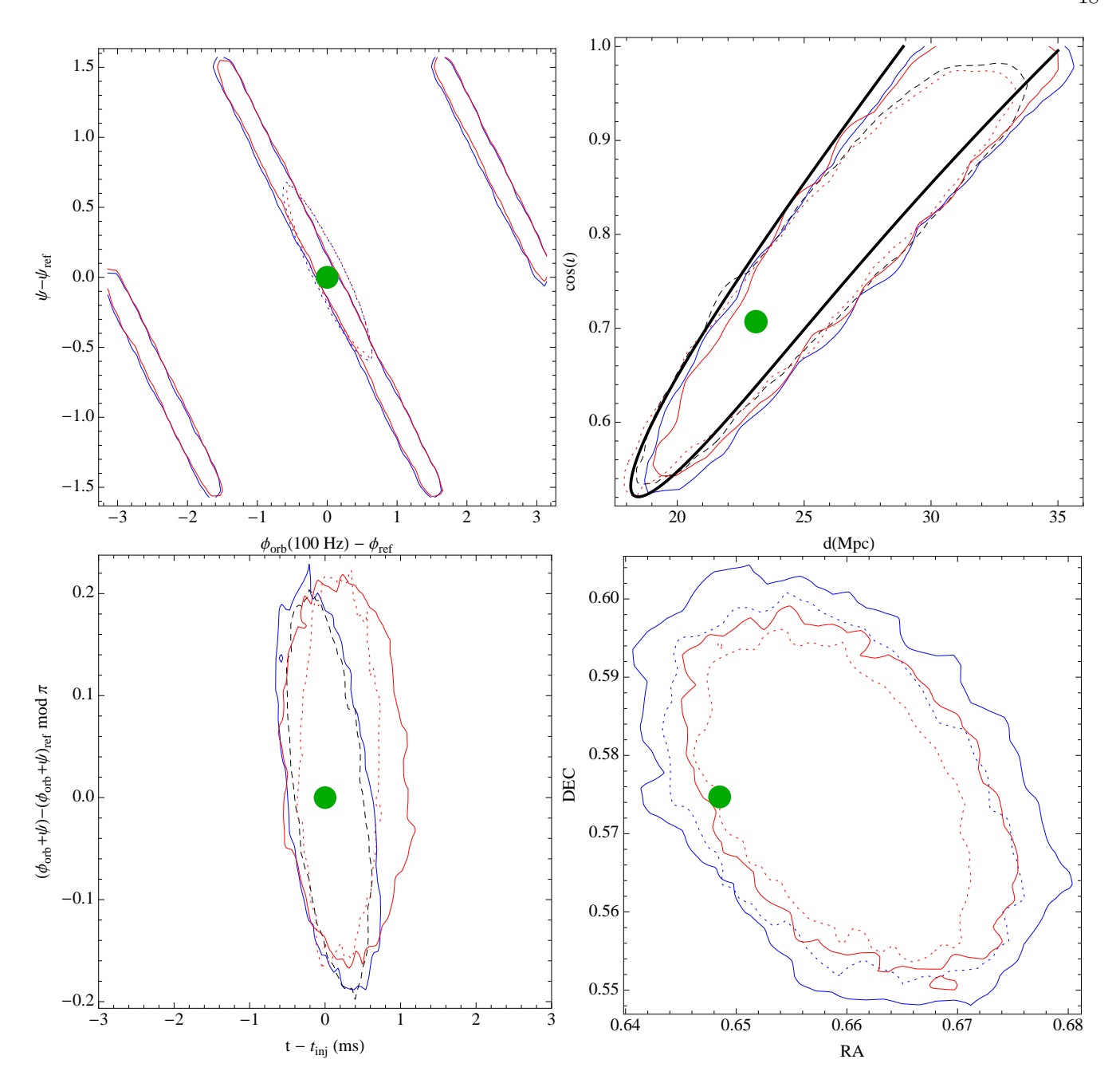


FIG. 4: Higher harmonics provide information about geometry: For zero-spin binaries (blue) and aligned-spin binaries (red), a comparison of 90% confidence intervals derived with and without higher harmonics (dotted, solid, respectively). Though the plotted results are obtained without noise, similar results are obtained with each noise realization Top left panel: Posterior in ψ (the angle of \hat{L} projected onto the plane of the sky) and $\phi_{\rm ref}$ (the orbital phase at 100 Hz). In the absence of higher harmonics, $\phi_{\text{ref}} + \psi$ is strongly constrained by observations but $\phi_{\text{ref}} - \psi$ is unconstrained. When higher harmonics are included, the range of possible values of $\phi_{\rm ref} - \psi$ is significantly reduced. Top right panel: Posterior in d (distance to the source) and $\cos \iota$ for ι the inclination. The heavy black curve shows an analytic approximation to the 90% confidence interval [Eq. (42)]. Except for limiting cases ($\cos \iota \simeq \pm 1,0$) or special sky locations, higher harmonics provide relatively little new information about the source orientation and distance. Our results are consistent with prior work [20, 21, 28, 61-63]. Bottom left panel: Posterior in $\psi + \phi_{\rm ref}$ versus $t - t_{inj}$. While higher harmonics improve our ability to measure the previously unconstrainted $\psi - \phi_{\rm ref}$, they do not significantly improve our ability to measure time or the other phase $(\phi_{ref} + \psi)$. Bottom right panel: Posterior distribution for the source position on the plane of the sky. Higher harmonics slightly improve our ability to isolate the direction to the source, reducing the 90% confidence interval sky area by tens of percent. The improved sky area is smaller only in part because higher harmonics increase the signal amplitude and thus improve our ability to identify the source's location. While a source with higher harmonics has larger amplitude (ρ^2 larger by about 3%), the increased amplitude alone does not explain the significantly smaller sky area. The center of our recovered distributions and the actual source sky location (green dot) are offset by about 0.01 rad. This is due to an error in the injection routines, see Footnote??.

| Source | Harmonics | Seed | $D_{KL}(\mathcal{M}_c, \eta)$ | $D_{KL}(\mathcal{M}_c, \eta \text{eff})$ | $D_{KL}(\mathcal{M}_c,\eta,\chi)$ | $D_{KL}(\mathcal{M}_c, \eta, \chi \text{eff})$ |
|--------------|-----------|--------|-------------------------------|---|-----------------------------------|--|
| Zero spin | no | - | 0.00128 | 0.0411 | | |
| Zero spin | no | _* | 0 | 0.0285 | | |
| Zero spin | no | 1234 | 0.0157 | 0.00261 | | |
| Zero spin | no | 1234* | 0.0321 | 0.0462 | | |
| Zero spin | no | 56789 | 0.0733 | 0.0193 | | |
| Zero spin | no | 56789* | 0.0209 | 0.0886 | | |
| Zero spin | with | - | 0.0229 | 0.0299 | | |
| Zero spin | with | _* | 0.0235 | 0.0339 | | |
| Zero spin | with | 1234 | 0.0718 | 0.00941 | | |
| Zero spin | with | 1234* | 0.00202 | 0.0338 | | |
| Zero spin | with | 56789 | 0.112 | 0.0288 | | |
| Zero spin | with | 56789* | 0.0305 | 0.122 | | |
| Aligned spin | no | - | 0.00391 | 0.0984 | 0.00427 | 2.29 |
| Aligned spin | no | -* | 0 | 0.123 | 0 | 2.31 |
| Aligned spin | no | 1234 | 0.0272 | 0.16 | 0.140 | 2.12 |
| Aligned spin | no | 1234* | 0.110 | 0.0959 | 0.163 | 2.07 |
| Aligned spin | no | 56789 | 1.17 | 0.44 | 1.82 | 2.13 |
| Aligned spin | no | 56789* | 0.0112 | 0.0971 | 0.0833 | 2.51 |
| Aligned spin | with | - | 0.216 | 0.0734 | 0.265 | 2.3 |
| Aligned spin | with | _* | 1.45 | 0.0733 | 1.68 | 2.21 |
| Aligned spin | with | 1234 | 0.512 | 0.0465 | 0.609 | 2.19 |
| Aligned spin | with | 1234* | 0.724 | 0.044 | 0.898 | 2.02 |
| Aligned spin | with | 56789 | 1.31 | 0.0807 | 3.10 | 1.8 |
| Aligned spin | with | 56789* | 0.0661 | 0.511 | 0.163 | 3.12 |

TABLE V: Comparing simulations: For each simulation, a comparison of that simulation's shape with either (a) some other similar simulation's shape (columns $D_{KL}(\mathcal{M}_c, \eta)$ and $D_{KL}(\mathcal{M}_c, \eta, \chi)$), either (zero spin, no, -*) or (aligned spin, no, -*), or (b) the corresponding effective Fisher matrix provided in Table VIII. For zero spin, the first three rows show differences consistent with noise fluctuations [Eq. (29)]; for aligned spin, diffrences are more substantial and coordinate-system dependent, but not above the conditions needed to distinguish between distributions [Eq. (30)].

significantly larger than this value; most notably, the zero spin 56789* realizations with and without noise have $\Delta \ln(V/V_{\rm prior}) \simeq -27.3 + 40.4 \simeq 13$. While these pairs of simulations have large prior volume differences, followup comparisons show no clear sign that higher harmonics have any significant impact. For example, these simulations have nearly regular one- and two-dimensional parameter distributions [Table IV and Figures 1 and 4]. Too, when the evidence is calculated using a different method, described in Appendix C, this discrepancy disappears. We suspect that direct evidence integration, the default method used in lalinference_mcmc and reported in Table IV, may behave pathologically for outlier noise realizations, particularly when an extremely low-probability secondary maxima is under-resolved in set of posterior samples. By contrast, in our experience, thermodynamic integration produces no extreme outliers, has V/V_{prior} consistently smaller for simulations with higher harmonics versus without, produces humanreadable intermediate output (i.e., the log-likelihood versus temperature), and has analytically-tractable limits; see Appendix C. Unfortunately, in our experience, thermodynamic integration also produces significantly different results for the absolute value of evidence Z and hence $V/V_{\rm prior}$. For the purposes of this work, however, the two methods qualitatively agree on evidence and $V/V_{\rm prior}$ differences and qualitatively support the conclusions drawn above. Our interpretation of these results is that the change in $V/V_{\rm prior}$ is smaller than the systematic error in the evidence ($\Delta \ln(V/V_{\rm prior}) \lesssim 5$); a significant fraction of that change is responsible for improving our understanding of one parameter; and the remainder is distributed across all other parameters, improving their measurement accuracy by tens of percent at best.

D. Posteriors separate into intrinsic and extrinsic variables, after maximizing in time and phase

COOKL claimed that the posterior for nonprecessing binaries largely separates into purely intrinsic and purely extrinsic parameters, even in the presence of higher harmonics, when the posterior is marginalized over polarization and event time. In Table VI, we use mutual information [Eq. (31)] to quantify correlations between intrinsic parameters (\mathcal{M}_c, η, a) and extrinsic parame

ters (ln L, cos ι , ϕ_{orb} , RA, DEC and t, ψ).¹⁷ To provide a sense of scale, we expect numerical and sampling error could introduce random values of $I \simeq 10^{-2} (N_{\rm eff}/10^4)^{-1}$ [Eq. (34)]. By contrast, a strongly-coupled Fisher and covariance matrix will have I greater than or of order unity [Eq. (31)].

When all intrinsic parameters are included in the covariance matrix, strong correlations exist between intrinsic and extrinsic parameters, as show by mutual information of order unity in the I(A,B+C) and I(A',B+C) columns. These correlations reflect the well-understood strong correlations between time, orbital phase, polarization, and the best-fitting intrinsic parameters. In fact, as claimed in COOKL, most correlations between intrinsic and extrinsic parameters are intimately tied to measuring time or phase. Marginalizing over these variables vastly reduces the correlations between intrinsic and the remaining extrinsic variables, both with and without spin, as can be seen by examining the $I(A,B+\psi)$ (marginalize over time) and I(A,B) columns (marginalize over time and phase).

V. COMPARING PARAMETER ESTIMATION TO THE EFFECTIVE FISHER MATRIX

A. Effective Fisher matrix predictions

COOKL calculated an effective Fisher matrix using a specific post-Newtonian approximation that neglected the quadrupole-monopole [64], self-spin [65] and 2.5PN spin-orbit terms¹⁸ [7, 66, 67]. These terms have since been added to the lalsimulation code, and so they are included in this work. Table VII provides a revised effective Fisher matrix, including their effect. Table VIII compares our revised effective Fisher matrix (with the new spin terms) in the aligned-spin case to the effective Fisher matrix computed with the older waveform model. The waveform model is unchanged for non-spinning binaries.

To provide a benchmark for comparison, we have calculated the KL divergence between the effective Fisher matrices derived with and without higher harmonics:

$$D_{KL}(\mathcal{M}_c, \eta | \text{zero spin}) = 0.019$$
 (39)

$$D_{KL}(\mathcal{M}_c, \eta | \text{aligned spin}) = 0.38$$
 (40)

$$D_{KL}(\mathcal{M}_c, \eta, \chi | \text{aligned spin}) = 0.46$$
 (41)

In other words, the effective Fisher matrix suggests higher harmonics will marginally influence the posterior correlations between intrinsic parameters, with shape changes comparable to the typical fluctuations between noise realizations seen in our study [Table V]. In the non-spinning case, both noise fluctuations and the influence of higher harmonics are small. When including spin as a parameter, both noise fluctuations and higher harmonics have a larger impact on the posterior shape.

B. Comparing predicted and calculated intrinsic parameter distributions

As described above, our simulations produce (one-, two-, and three-dimesional) posterior distributions of intrinsic parameters that are similar to one another. The heavy black solid and dotted curves in Figures 1 and 3 compare the predictions of the effective Fisher matrix, scaled to $\rho = 20$, to the results of our simulations. Table V provides a quantitative comparison between each two- and three-dimensional covariance matrix Σ_{ab} and the corresponding two- and three-dimensional effective Fisher matrix K_* , via D_{KL} [Eq. (23)]. For a sense of scale, any two two-dimensional Monte Carlo posteriors that sample the same distribution should differ by less than $D_{KL} \simeq 2 \times 10^{-3}$ [Eq. (27)], while any two independent noise realizations should have two-dimensional posteriors which differ by less than $D_{KL} \simeq 0.015$ [Eq. (30)].

In the absence of spin, as demonstrated qualitatively via the heavy black curves in Figure 1 and quantitatively by the D_{KL} in Table V, our effective Fisher matrix predictions agree remarkably well with the simulated results, despite the substantial simplifications they employ.

By contrast, when spin is included as a parameter, the predictions of the effective Fisher matrix seem to fare more poorly, particularly in capturing multiparameter correlations; see the heavy black curves in Figure 3. To some extent, as anticipated in Section IIID our poor performance reflects poorly chosen coordinates. In our coordinates, the confidence intervals are long and non-ellipsoidal, being distorted by significant changes to the metric across substantial ranges of parameter space, whereas the effective Fisher matrix contours are always ellipsoidal by construction. The large D_{KL} values provided in Table V for aligned-spin binaries indicate that the effective Fisher matrix and simulations have covariances with different principal axes. Due to the extremely large ratio of eigenvalues in three dimensions ($\simeq 10^5$), even an extremely small relative misalignment θ between the predicted and simulated correlation leads to a large $D_{KL} \simeq 10^5 \theta^2$. To a lesser extent, both the one and twodimensional correlations are negatively influenced by the hard cutoff in χ . Given the sensitivity of D_{KL} to misalignment, one could argue that the COOKL procedure is performing rather well even for the aligned-spin case.

¹⁷ From experience and following prior work, we change variables, eliminating distance in favor of the signal amplitude ρ .

¹⁸ But again, we have not included 3PN and 3.5PN SO terms, which were implemented in lalsimulation after this work as well underway.

| Source | Harmonics | Seed | I(A, B+C) | $I(A, B + \psi)$ | I(A,B) | I(A', B+C) | $I(A', B + \psi)$ | I(A',B) |
|--------------|-----------|--------|-----------|------------------|--------|------------|-------------------|---------|
| Zero spin | no | - | 0.87 | 0.02 | 0.02 | - | - | - |
| Zero spin | with | - | 0.76 | 0.02 | 0.02 | - | - | - |
| Zero spin | no | -* | 0.86 | 0.01 | 0.01 | - | - | - |
| Zero spin | with | _* | 0.78 | 0.06 | 0.02 | - | - | - |
| Zero spin | no | 1234 | 0.78 | 0.01 | 0.01 | - | - | - |
| Zero spin | with | 1234 | 0.68 | 0.04 | 0.04 | - | - | - |
| Zero spin | no | 1234* | 0.92 | 0.04 | 0.04 | - | - | - |
| Zero spin | with | 1234* | 1.61 | 0.68 | 0.05 | - | - | - |
| Zero spin | no | 56789 | 0.83 | 0.01 | 0.01 | - | - | - |
| Zero spin | with | 56789 | 0.69 | 0.04 | 0.04 | - | - | - |
| Zero spin | no | 56789* | 0.97 | 0.09 | 0.09 | - | - | - |
| Zero spin | with | 56789* | 1.06 | 0.25 | 0.16 | _ | | |
| Aligned spin | no | - | 0.84 | 0.08 | 0.06 | 0.94 | 0.06 | 0.06 |
| Aligned spin | with | - | 1.08 | 0.52 | 0.04 | 0.75 | 0.09 | 0.05 |
| Aligned spin | no | _* | 0.86 | 0.05 | 0.05 | 0.99 | 0.05 | 0.05 |
| Aligned spin | with | _* | 1.13 | 0.53 | 0.04 | 0.79 | 0.09 | 0.05 |
| Aligned spin | no | 1234 | 0.91 | 0.16 | 0.14 | 0.99 | 0.15 | 0.15 |
| Aligned spin | with | 1234 | 1.58 | 1.11 | 0.09 | 0.77 | 0.21 | 0.06 |
| Aligned spin | no | 1234* | 0.75 | 0.06 | 0.06 | 0.84 | 0.06 | 0.06 |
| Aligned spin | with | 1234* | 1.56 | 1.06 | 0.10 | 0.77 | 0.20 | 0.06 |
| Aligned spin | no | 56789 | 0.68 | 0.09 | 0.06 | 0.72 | 0.06 | 0.06 |
| Aligned spin | with | 56789 | 2.24 | 1.50 | 0.23 | 1.31 | 0.56 | 0.15 |
| Aligned spin | no | 56789* | 0.66 | 0.03 | 0.03 | 0.78 | 0.03 | 0.03 |
| Aligned spin | with | 56789* | 1.13 | 0.38 | 0.18 | 1.08 | 0.17 | 0.17 |

TABLE VI: Mutual information between intrinsic and extrinsic variables tied to time and phase: The mutual information I between intrinsic variables (represented as either $A \equiv (\tau_0, \tau_3)$ or $A' = A + \chi$) and extrinsic variables (represented as either $B = (d_L, \cos \iota, \phi_{orb}, RA, DEC)$ or some of $C = (t, \psi)$). After marginalizing over time and/or phase, covariances have extremely weak correlations between extrinsic and intrinsic parameters.

| Source | | | Zero sp | oin | | Aligned spin | | | | | | |
|--------------------------------------|-------------|-------------|---------|-------------|--------|--------------|--------|--------|-------------|--------|--------|--|
| Harmonics | | no | | | ith | | no | | with | | | |
| Parameter | | $M_{\rm c}$ | η | $M_{\rm c}$ | η | $M_{\rm c}$ | η | χ | $M_{\rm c}$ | η | χ | |
| | $M_{\rm c}$ | 5688 | -8900 | 6017 | -9611 | 6044 | -246.5 | -1414 | 7073 | -603.8 | -1718 | |
| $(\hat{\Gamma}_{ij})_{\mathrm{eff}}$ | η | - | 15197 | - | 16928 | - | 379.9 | 146.8 | - | 646.2 | 275.0 | |
| | χ | - | - | - | - | - | - | 354.3 | - | - | 448.1 | |
| | $M_{\rm c}$ | 1.00 | 0.957 | 1.00 | 0.952 | 1.00 | -0.950 | 0.997 | 1.00 | -0.936 | 0.995 | |
| c_{ij} | η | - | 1.00 | - | 1.00 | - | 1.00 | -0.957 | - | 1.00 | -0.949 | |
| | χ | - | - | - | - | - | - | 1.00 | - | - | 1.00 | |
| $\sigma_i \times 10^3$ | | 2.29 | 1.40 | 2.11 | 1.26 | 7.98 | 8.94 | 35.5 | 6.44 | 6.49 | 28.5 | |
| γ_i | | 20533 | 352.34 | 22524 | 420.43 | 6389 | 387.9 | 1.792 | 7553 | 610.9 | 2.798 | |

TABLE VII: Effective fitting parameters: Following the tables in COOKL, this table provides $\hat{\Gamma}_{\text{eff}}$, a locally quadratic fit to a specific, idealized ambiguity function (the "effective Fisher matrix"); the correlation coefficients derived from $\hat{\Gamma}_{\text{eff}}$; the eigenvalues of $\hat{\Gamma}$; and the one-dimensional covariances $\sigma_a = \sqrt{\Sigma_{aa}}$ for $\Sigma = (20)^2 \hat{\Gamma}_{\text{eff}}$. Including many more significant figures than shown above, the data used in our own calculations is available on request. Due to the orders-of-magnitude difference between eigenvalues (γ_i) shown, many significant figures are required to reproduce our calculations in full.

C. Geometric parameters

not be captured with a locally Gaussian approximation in conventional coordinates. Nonetheless, the posterior over geometric parameters can be well-approximated us-

Including source orientation and distance, the posterior is well-known to have several correlations which can-

ing a few simple network-independent expressions:

$$A(\theta) \equiv \sqrt{|Y_{22}^{(-2)}(\theta,0)|^2 + |Y_{2,-2}^{(-2)}(\theta,0)|^2}$$
(42a)
$$\frac{dp(r,\iota)}{dr d\cos\iota} \propto r^2 e^{-\frac{\rho^2}{2} \left[1 + \frac{A(\iota)^2}{A(\pi/4)^2 (r/d_0)^2} - 2P(\iota,\pi/4) \frac{A(\iota)}{A(\pi/4)(r/d_0)} \right]}$$
(42b)

where P, an inner product evaluated over all orientations, is provided by Eq. (28) in COOKL. The seemingly-complicated expression appearing in the exponential is nothing more than

$$\frac{1}{2} \left[\langle h|h\rangle + \langle h'|h'\rangle - 2\langle h|h'\rangle \right] \tag{43}$$

evaluated by re-expressing $h' = \rho \hat{h}' A(\iota) / A(\pi/4)$ where h' is normalized $(\langle \hat{h}' | \hat{h}' \rangle = 1)$; performing a similar replacement for h; and replacing the overlap $\langle \hat{h} | \hat{h}' \rangle$ between normalized complex-valued states by P. As illustrated using one contour (the heavy black curve) in Figure 4, this distribution accurately approximates the source distance and orientation posterior in the absence of higher harmonics. This agreement occurs despite considerable differences in the two models: our simulations use a realistic three-detector configuration and include all correlations with sky position, while COOKL assume an idealized network and omit any correlation with sky location.

Similar network-independent approximations can reproduce features seen in other correlations. As a concrete example, using a well-chosen reference frequency we expect and Figure 4 confirms that the posterior in ψ , $\phi_{\rm ref}$ is concentrated near hyperplanes of either constant $\psi_{\pm} \equiv \psi \pm \phi_{\rm ref}$, depending on which harmonic dominates. Specifically, in the absence of higher harmonics, the marginalized posterior $p(\psi_+, \psi_-)d\psi_+d\psi_-$, defined by marginalizing all other degrees of freedom

$$p(\psi_{+}, \psi_{-})d\psi_{+}d\psi_{-} \equiv \int_{\lambda} p(\psi, \phi_{\text{ref}}, \lambda)d\lambda \qquad (44)$$

can be approximated by a one-dimensional Gaussian distribution depending on either ψ_+ or ψ_- , in the neigborhood of one such hyperplane. For the solid curves shown in the top left panel of Figure 4 and the covariance provided in Table IV, a good local approximation is given by

$$p(\psi_+) \propto e^{-\rho^2 \bar{\Gamma}_{++} \delta \psi_+^2/2}$$
 for this case (45a)

$$\bar{\Gamma}_{++} \equiv -\frac{2}{\rho^2} \partial_{\psi_{+}}^2 \ln \int \int_{\lambda} p(\psi, \phi_{\text{ref}}, \lambda) d\lambda$$
 (45b)

In the large-signal-amplitude limit, we can calculate $\bar{\Gamma}_{++}$ by using the known functional form of the waveform emitted along the orbital angular momentum direction $h(t, \hat{z}, \lambda)$ on all intrinsic parameters:

$$\bar{\Gamma}_{++} = 4 - \sum_{ab \neq \psi} \Gamma_{\psi a} \Gamma_{\psi b} [\Gamma_{ab}]^{-1}
= 4 - 4 \frac{\langle \partial_a h | h \rangle \langle \partial h | \partial h \rangle_{ab}^{-1} \langle h | \partial_b h \rangle}{\rho^2}$$
(46)

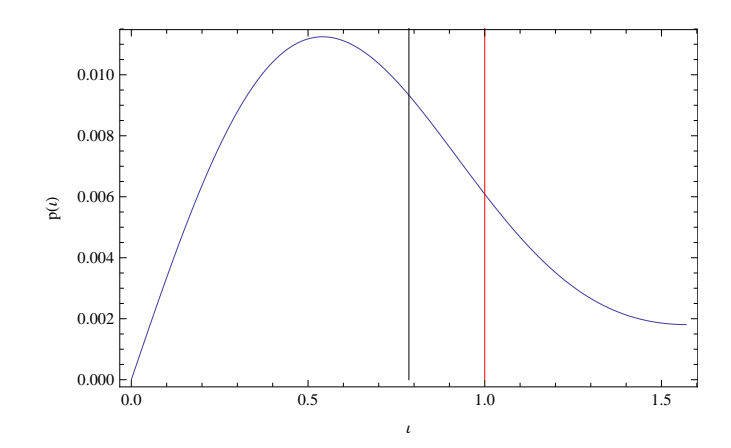


FIG. 5: Reference inclination is typical: The vertical black line shows the source inclination ($\iota = \pi/4$) adopted in this work. For comparison, the curve shows the relative probability $p(\iota) \propto \int d\phi |h(\iota,\phi)|^3 \sin \iota$ of different inclinations ι for a binary detected by an idealized network with isotropic sensitivity to both polarizations. Finally, the red line at $\iota \simeq 1$ indicates the approximate angle above which both the (2,2)and (2,-2) modes influence the signal amplitude by more than a fractional change in $1/\rho^2$ for $\rho \simeq 20$; for inclinations smaller than the red line, the signal can be described as nearly circularly polarized for network amplitudes $\rho \lesssim 20$. Source inclinations closer to $\iota \simeq 0, \pi$ will be even better described by a single circular polarization than the systems explored in this work. By contrast, the $\simeq 18\%$ of all orientations between $\iota \simeq 1$ and $\pi - 1$ contain significant contributions from both left- and right-handed emission.

where $[\Gamma_{ab}]^{-1} = \langle \partial h | \partial h \rangle_{ab}^{-1}$ is the inverse of the submatrix not involved with ψ_{\pm} . For the post-Newtonian approximation adopted in the text, we find $\bar{\Gamma}_{++} \simeq 0.27 - 0.28$, which adequately reproduce the observed widths in Table IV and Figure 4: $\sigma_{+} \simeq 1/\sqrt{\bar{\Gamma}\rho^{2}} \simeq 0.095$. This approximation holds independent of the network's relative sensitivity to the two polarizations. Finally and similarly, the posterior probability distribution in t and ψ_{+} can be approximated by a Gaussian.

Our ability to correctly reproduce the source orientation distribution, as well as to correctly model the intrinsic parameter distribution of nonspinning binaries, suggests that the COOKL approach correctly approximates the posterior distribution. In particular, for the examples shown here, multidetector physics is not needed to model the posterior distribution to a zeroth approximation.

¹⁹ To a first approximation, the signal can be approximated as circularly polarized; the relative sensitivity to one or another linear polarization is irrelevant.

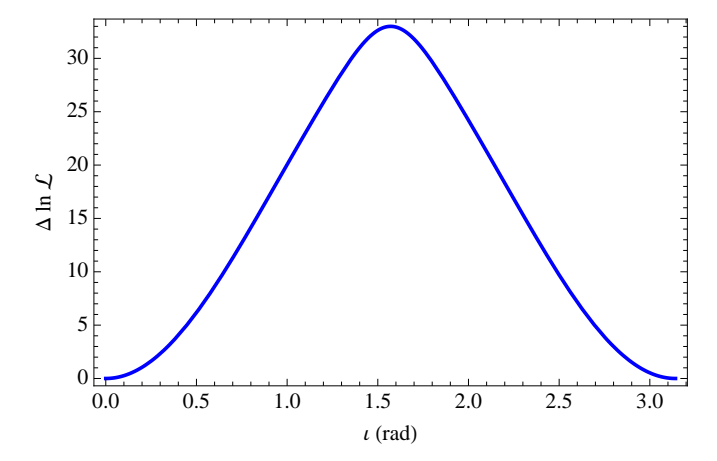


FIG. 6: Influence on higher harmonics with inclination: Here we plot the expected change in max log-likelihood from the inclusion of higher harmonics $\Delta \ln \mathcal{L} = \rho_{0PN}^2 \Delta \ln \rho^2/2$ vs inclination (ι), see Eq. (50). We assume all other parameters are those of our fiducial non-spinning binary. From our rule-of-thumb criteria $\Delta \ln \mathcal{L} \gtrsim 1$, we expect higher harmonics to have a significant effect on our recovered posterior except when the binary is very nearly face-on.

VI. GENERALIZING THE RESULTS

Though we present a detailed analysis of only two specific systems, certain aspects of our results can be generalized to make inferences about the parameter estimation prospects for a broader range of binary systems. In this section, we argue that the binary location and orientation we consider are, in a sense, "typical" of detectable binaries.

As gravitational wave emission is strongest along the orbital angular momentum axis, most nonprecessing binaries will be detected nearly face on and hence be dominated by circularly-polarized emission. The inclination distribution for detected, nonprecessing binaries, which follows from Eq. 42, is plotted in Fig. 5. This figure shows that the distribution is strongly biased towards small inclination. By contrast, higher harmonics have their greatest impact near the orbital plane, since the odd harmonics are proportional to $\sin \iota$.

We expect that higher harmonics can have a significant influence on the posterior if they changes the max log-likelihood ratio by $\gtrsim 1$. From Eq. (19), this is equivalent to increasing the square of SNR by $\gtrsim 2$. We have the following formulae for the SNR-squared from restricted waveforms, from first-order amplitude-corrected waveforms, and the fractional increase from amplitude cor-

rections:

$$\rho_{0PN}^{2} = ||h_{22}||^{2} \left(\left| Y_{22}^{(-2)} \right|^{2} + \left| Y_{2-2}^{(-2)} \right|^{2} \right), \quad (47)$$

$$\rho_{0.5PN}^{2} = \rho_{0PN}^{2} \left(1 + \Delta \ln \rho^{2} \right), \quad (48)$$

$$\Delta \ln \rho^{2} = \frac{1}{\rho_{0PN}^{2}} \left[||h_{21}||^{2} \left(\left| Y_{21}^{(-2)} \right|^{2} + \left| Y_{2-1}^{(-2)} \right|^{2} \right) + ||h_{33}||^{2} \left(\left| Y_{33}^{(-2)} \right|^{2} + \left| Y_{3-3}^{(-2)} \right|^{2} \right) + ||h_{31}||^{2} \left(\left| Y_{31}^{(-2)} \right|^{2} + \left| Y_{3-1}^{(-2)} \right|^{2} \right) \right]. \quad (49)$$

Note that $||h_{\ell m}||^2 \equiv \langle h_{\ell m}|h_{\ell m}\rangle$, we have used the fact that $||h_{\ell-m}||^2 = ||h_{\ell m}||^2$, and we have assumed that different $h_{\ell m}$ modes are orthogonal.²⁰ The fractional increase in SNR can be written as a combination of prefactors, a ratio of frequency moments of the PSD, and ratios of $Y_{\ell m}^{(-2)}$'s to make the dependence on inclination and mass parameters more explicit. In particular,

$$\Delta \ln \rho^2 = \mathcal{I} \left[\frac{1}{9} \mathcal{Y}(2,1) + \frac{135}{224} \mathcal{Y}(3,3) + \frac{1}{2016} \mathcal{Y}(3,1) \right], \tag{50}$$

with

$$\mathcal{I} = (\pi M)^{2/3} \delta^2 \frac{\int \frac{f^{-5/3}}{S_n(f)} df}{\int \frac{f^{-7/3}}{S_n(f)} df} \simeq 0.05 , \quad (51)$$

$$\mathcal{Y}(\ell,m) = \frac{\left|Y_{\ell m}^{(-2)}(\iota,0)\right|^2 + \left|Y_{\ell - m}^{(-2)}(\iota,0)\right|^2}{\left|Y_{22}^{(-2)}(\iota,0)\right|^2 + \left|Y_{2-2}^{(-2)}(\iota,0)\right|^2} . \quad (52)$$

where $\delta = (m_1 - m_2)/M = \sqrt{1 - 4\eta}$ and the approximate numerical value for \mathcal{I} was computed assuming our initial LIGO and Virgo three-detector network. The \mathcal{Y} functions appearing in Eq. (50) all peak at $\iota = \pi/2$, are symmetric about that point, and approach zero as $\iota \to 0, \pi$.

We can write our condition for when higher harmonics to significantly affect the posterior as $\Delta \ln \mathcal{L} = \rho_{0PN}^2 \Delta \ln \rho^2/2 \gtrsim 1$. Eqs. (50)-(52) quantify how the influence of higher harmonics scales with inclination, mass ratio and total mass, showing that they become less important for face-on, nearly equal mass and lower total mass, as is well known. Higher harmonics can influence our posterior for almost any inclination, so long as ι is in the approximate range $[0.1,\pi-0.1],$ as illustrated in Fig. 6.

For the sky location of our binary, we intentionally chose a location so that the signal amplitude at each detector site was of comparable strength. To demonstrate our source sky location was representative, we distributed

²⁰ This assumption works very well for the masses considered here, but may break down at very high mass, when the modes may be only a few cycles long.

each of 10⁶ points distributed uniformly across the sky and evaluated the optimality of orientation for each detector in the network at that sky location. Specifically, for each sky location, we compute the "amplitude factor" at each of the LIGO and Virgo detector sites

$$0 \le A \equiv \sqrt{F_{+}^{2} \frac{1}{4} (1 + \cos^{2} \iota)^{2} + F_{\times}^{2} \cos^{2} \iota} \le 1.$$
 (53)

Used in the "effective distance", this expression is the ratio of the observed signal amplitude in a detector to the amplitude of the same signal if it were optimally oriented. The values A_1 , A_2 and A_3 denote the amplitude factors of the first-, second- and third-best oriented detectors. So, for example, $A_2/A_1 = 0.5$ ($A_3/A_1 = 0.5$) means that the signal was half as loud in the second- (third-) best detector as it was in the most favorably oriented one. In Fig. (7), we plot the cumulative histograms of A_2/A_1 and A_3/A_1 . The vertical lines represent the values of these ratios for our injected signals (roughly 0.8 and 0.7, respectively). First, note that the amplitude factor ratios of our injected signals are quite close to the mean of the distribution. In addition, the second- (third-) best oriented detector will have at least half the signal amplitude of the best oriented detector for 90% (70%) of the sky. Comparable angular response A_k in all detectors is the norm; a signal in the blind spot of one or more detectors is the exception. Note that we have carefully framed this point in terms of an amplitude factor which does not refer to the PSD of any detector. If, for example, one detector is far less sensitive than the others then one would get the best parameter estimation performance when both of the sensitive detectors have large amplitude factors, with little regard for the amplitude factor in the insensitive detector. At any rate, our main point is that the location and orientation of our fiducial signal is not in the blind spot of any detector in the LIGO-Virgo network, and that this will be the case for the majority of signals. This is true irrespective of the relative sensitivity of each detector in the network.

VII. CONCLUSIONS

In this work we investigate the prospects of parameter estimation for gravitational waves from BH-NS binaries. We perform full Markov-chain Monte Carlo parameter estimation studies with simulated Gaussian noise for the three-detector network of the initial LIGO and Virgo interferometers. Additionally, we predict the performance of these full parameter estimation runs using a simple analytic estimate based on an effective Fisher matrix method for an idealized detector network. We generally find that the effective Fisher matrix predictions agree with the full parameter estimation results to a reasonable accuracy.

Our primary conclusion is that amplitude corrections do not significantly improve the measurement of the

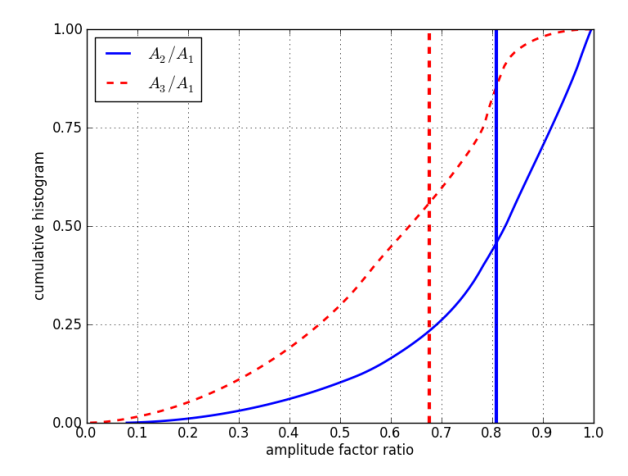


FIG. 7: Amplitude factor ratios versus sky location: We compute the amplitude factor (see Eq. (53)) of each LIGO and Virgo detector for a uniformly distributed set of sky locations and plot a cumulative histogram of the ratios A_2/A_1 (solid blue curve) and A_3/A_1 (dashed red curve), which tell us the signal amplitude of the second- and third-best oriented detectors, relative to the best oriented detector. The vertical lines denote these ratios for our injected signals. These results show that comparable signal amplitude in two and three detectors will be common for the LIGO-Virgo network, and that this network's sensitivity to our injection is typical.

masses and spins of the binary. Instead, their main effect is to improve the measurement of the astrophysically uninteresting source orientation, by breaking an approximate degeneracy between polarization angle and binary orbital phase at some reference point. By contrast, black hole spin is highly degenerate with all astrophysically interesting parameters (e.g., masses) and must be included and carefully calibrated, given the significant systematic uncertainties in spinning waveforms [68].

We use several analytic tools to study the posterior distributions of our MCMC results and compare them to the effective Fisher distribution. By computing a prior volume ratio, we argue that higher harmonics principally break the $\psi-\phi_{\rm ref}$ degeneracy, providing marginal improvements in the measurements of other parameters. By computing D_{KL} , a form of the KL-divergence, we conclude that our MCMC results for different noise realizations are self-consistent, and consistent with the effective Fisher matrix predictions. Using the mutual information, we show that the intrinsic parameters decouple from the extrinsic parameters after marginalizing over time and polarization angle.

While the results presented here are limited to a single mass ratio, binary location and orientation, we argue that they can be generalized to describe parameter estimation performance for a broader class of BH-NS signals. In particular, we show that the sky location of our signal is "typical", and that the LIGO-Virgo detector network would have a similar response (in which all three detec-

tors have a comparable signal strength) across a very large fraction of the sky. In addition, we show that the binary inclination to line of sight we considered is typical of detectable signals, and we show approximately but quantitatively how the importance of higher harmonics will vary with SNR and inclination.

We propose the use of the effective Fisher matrix, as applied in COOKL, as a computationally efficient way to predict parameter estimation performance, to suggest which physical effects are most important to include in waveform models for various regions of parameter space, and to provide guidance about the capabilities of future detectors.

Our study also introduces the prior volume $V/V_{\rm prior}$, a powerful global tool to assess when the data constrains additional parameters. The application of $V/V_{\rm prior}$ requires considerable care, being derived from the sometimes difficult-to-compute evidence Z. Any study of subdominant degrees of freedom in gravitational wave astronomy can adopt the tools presented here $(V/V_{\rm prior})$ and D_{KL} to assess whether new physics is accessible (e.g., modifications of gravity; spin-orbit misalignment) and if so precisely what information those new parameters provide.

Lastly, we make a somewhat technical point about the computational cost of performing parameter estimation with amplitude corrected waveforms. To fully and correctly include the effect of amplitude corrections requires a higher sampling rate and a lower starting frequency than restricted waveforms, which can significantly increase the computational cost of using amplitude corrected waveforms in parameter estimation. Using the same sample rate and starting frequency for amplitude corrected waveforms as for restricted waveforms will result in aliasing and missing low-frequency portions of the higher harmonics. However, we find that such effects have a minimal impact on the recovered posterior distributions, and so one could reasonably perform parameter estimation with amplitude corrected waveforms for the same computational cost as restricted waveforms.

Appendix A: Comparing two distributions' shapes

In the text, we use an extremely simple diagnostic to distinguish between two distributions: their covariance matrix. For any two nearly-Gaussian distributions characterized by K, so each has the form

$$p_{orig}(x|\mu, K) = \frac{|K|^{1/2}}{(2\pi)^{d/2}} e^{-(x-\mu)K(x-\mu)/2}$$

in the neighborhood of some mean, we have

$$D_{KL} \equiv \int p_* \ln p_*/p$$

$$= \frac{1}{2} \int p \left[\ln[|K_*|/|K|] - (x - \mu)K(x - \mu) + (x - \mu_*)K_*(x - \mu_*) \right]$$

$$= \frac{1}{2} \left[\ln[|K_*|/|K|] + (\mu - \mu_*)K_*(\mu - \mu_*) + \text{Tr}[(K_* - K)K_*^{-1}] \right] .$$
(A2)

In this work, we parallel-transport both distributions to a common mean; we therefore neglect the middle term in the above expression.

suitable rotation group generators, then

$$D_{KL}(K_*, K) = \frac{1}{2} \text{Tr}[K_*^{-1} R K_* R^{-1} - \mathbf{1}]]]$$

$$\simeq \frac{1}{2} \text{Tr}[-i\theta^k K_*^{-1} [L_k, K_*]$$

$$-\frac{1}{2} \theta_k \theta_q K_*^{-1} [L_k, [L_q, K_*]] + \dots]$$

$$\simeq \frac{1}{4} \text{Tr}[\theta_k \theta_q K_*^{-1} [L_k, [L_q, K_*]] + \dots] \quad (A3)$$

While the KL divergence has many desirable statistical properties, for our purposes, the greatest utility of the KL divergence is the ease with which Eq. (A2) can be evaluated and interpreted, allowing us to employ concrete examples to characterize what factors produce a large D_{KL} . For example, if K_* and K are related by a rotation $R = \exp(-i\theta^k L_k)$ through a small angle θ_k , where L_k are

because the rotation group generators L_k are traceless. Combined with the concrete example provided in the text, this general expression suggests that in many dimensions D_{KL} is extremely sensitive to small misalignments between K, K_* , scaling as $\theta^2 \lambda_+ / \lambda_-$ for λ_{\pm} the largest and smallest eigenvalues of K_* , respectively.

Appendix B: Sensitivity to PN model, sampling rate and starting frequency

It is well-known that the agreement between various PN waveform models is not perfect, and that these differences can lead to biases in recovered parameters, for example see [4]. A detailed study of the biases from waveform uncertainty is beyond the scope of this work. However, we do offer up an example of the level to which waveform systematics can influence our results. In particular, our current estimate for the effective Fisher matrix differs from the original COOKL result, because we adopt an updated model for how the spin influences the orbit. Table VIII provides our revised effective Fisher matrix. Implicitly, this table illustrates how sensitively our results depend on post-Newtonian order, particularly spin effects.

The calculations provided in the main text were performed with 4096 Hz sampling. Ideally, the sample rate used should be high enough such that the Nyquist frequency is greater than the highest frequency obtained by the highest harmonic in the waveform. provides the highest gravitational frequency from the leading-order quadrupole emission. When higher harmonics are included, we should sample at a substantially higher frequency, in direct proportion to the harmonics used. In particular, the spin-aligned waveform with higher harmonics contains a physical signal up to $(5/2) \, 1926 \, \text{Hz} \simeq 4815 \, \text{Hz}$, and so 16384 Hz is the lowest power-of-two sampling which will completely avoid any aliasing. Unfortunately for lalinference_mcmc, the computational cost of likelihood evaluations is proportional to the number of waveform samples, and thus increases linearly with the sampling rate.

Furthermore, the waveform length scales with the lower frequency as $f_{\rm low}^{-8/3}$ (see Eq. (5)). Therefore, a waveform for which the 5th harmonic is present all the way down to $f_{\rm low}$ will be a factor $(5/2)^{-8/3} \simeq 11.5$ longer than an equivalent waveform for which we only need the 2^{nd} harmonic down to $f_{\rm low}$. Therefore, starting at a sufficiently low frequency such that all higher harmonics are entirely in-band can increase the cost of both waveform generation and likelihood evaluations by more than an order of magnitude! As described in Sec. II A, we generate longer waveforms such that the highest $(5^{\rm th})$ harmonic is entirely in-band.

Are such expensive computations necessary to resolve the marginal impact from higher harmonics? To estimate how much sampling rate and lower frequency impacts our results, we calculated the local ambiguity function versus intrinsic parameters for the zero spin binary following COOKL, for several choices of sampling rate and lower frequency limit in Figure 8.

For the initial LIGO noise curve, we found that $f_{\rm min} \geq 30\,{\rm Hz}$ and $f_{\rm samp} > 2\,$ kHz was required for zero spin templates, with and without higher harmonics. In the case of aligned spin, although the theoretical lower limit of the sampling rate is 16384 kHz for the higher order

waveforms, we found that the local ambiguity function was well recovered by using the sampling rate of 4096 kHz. Moreover, as demonstrated in the text, this sampling rate produces good agreement with our theoretical predictions. Conversely, to illustrate the pathologies that arise when undersampling a signal, we have performed simulations with $f_{\rm samp}=1\,{\rm kHz}$. Despite the aliasing high of physical frequencies, the detectors' poor sensitivity to high frequencies could de facto allow computation at such a low sampling rate. Despite the relatively small amount of signal power associated with high frequency, aliasing produced noticable modulations and biases in our posteriors. No lower sampling rate should be employed, without explicitly filtering away high frequency content.

Appendix C: Effective dimension and prior volume versus signal amplitude

Parallel-tempered markov-chain Monte Carlo has been described at length before, both in general [69, 70] and in the context of ground- and space-based gravitational wave astronomy; see, e.g., [71–74] [15–21] and references therein. In this appendix, we describe how we reprocessed the multiple MCMC chains to evaluate the effective dimension (D_{eff}) . As described in the text, the excellent agreement between our numerical result and the theoretically-expected value for this quantity gave us additional confidence our simulations had converged. Inevitably, we also touch upon an independent method we adopted to evaluate the evidence (thermodynamic integration). As described in the text, relatively accurate evidence integrals were critical in allowing us to rule out significant impact of higher harmonics beyond the relatively trivial effect described in the text.

1. Review of parallel tempering and thermodynamic integration

The lalinference_mcmc code evolves several parallel MCMC chains simultaneously, each with a likelihood of the form

$$\mathcal{L}(\beta) \equiv \mathcal{L}^{\beta} \tag{C1}$$

where $T=1/\beta$ is called the chain's "temperature". The low-temperature likelihoods resemble our targeted, physical distribution while high-temperature likelihoods correspond to weaker signal strength and enable efficient exploration of the entire parameter space.

Theoretically speaking, parallel-tempered chains allow us to calculate the evidence Z [Eq. (15)] and $V/V_{\rm prior}$ [Eq. (17)] using "thermodynamic integration" [52]. Thermodynamic integration for the evidence relies

| Waveform | | | | Previo | ous | | | Current | | | | | | |
|-----------------------------------|-------------|-------------|--------|--------|-------------|--------|--------|-------------|--------|--------|-------------|--------|--------|--|
| Harmonics | | no | | | with | | | | no | | with | | | |
| Parameter | | $M_{\rm c}$ | η | χ | $M_{\rm c}$ | η | χ | $M_{\rm c}$ | η | χ | $M_{\rm c}$ | η | χ | |
| $(\hat{\Gamma}_{ij})_{	ext{eff}}$ | $M_{\rm c}$ | 5935 | -1821 | -1431 | 6598 | -2335 | -1631 | 6044 | -246.5 | -1414 | 7073 | -603.8 | -1718 | |
| | η | - | 1381 | 559.3 | - | 1961 | 731.9 | - | 379.9 | 146.8 | - | 646.2 | 275.0 | |
| | χ | - | - | 364.2 | - | - | 426.1 | - | - | 354.3 | - | - | 448.1 | |
| | $M_{\rm c}$ | 1.00 | -0.939 | 0.995 | 1.00 | -0.929 | 0.994 | 1.00 | -0.950 | 0.997 | 1.00 | -0.936 | 0.995 | |
| c_{ij} | η | - | 1.00 | -0.962 | - | 1.00 | -0.957 | - | 1.00 | -0.957 | - | 1.00 | -0.949 | |
| | χ | - | - | 1.00 | - | - | 1.00 | - | - | 1.00 | - | - | 1.00 | |
| $\sigma_i \times 10^3$ | | 8.27 | 6.36 | 41.9 | 7.14 | 5.09 | 35.7 | 7.98 | 8.94 | 35.5 | 6.44 | 6.49 | 28.5 | |
| γ_i | | 6933 | 746.1 | 1.343 | 7992 | 991.5 | 1.856 | 6389 | 387.9 | 1.792 | 7553 | 610.9 | 2.798 | |

TABLE VIII: Sensitivity of (effective) Fisher matrix to post-Newtonian approximation, SNR=20: The columns labeled "Previous" give the effective Fisher matrix and expected parameter errors for the waveforms used in [22]. The columns labeled "Current" give the same results for waveform which contain additional spin-dependent phasing corrections (as explained in Sec. VA). The effective Fisher matrix inevitably depends on the still-uncertain post-Newtonian waveform model used.

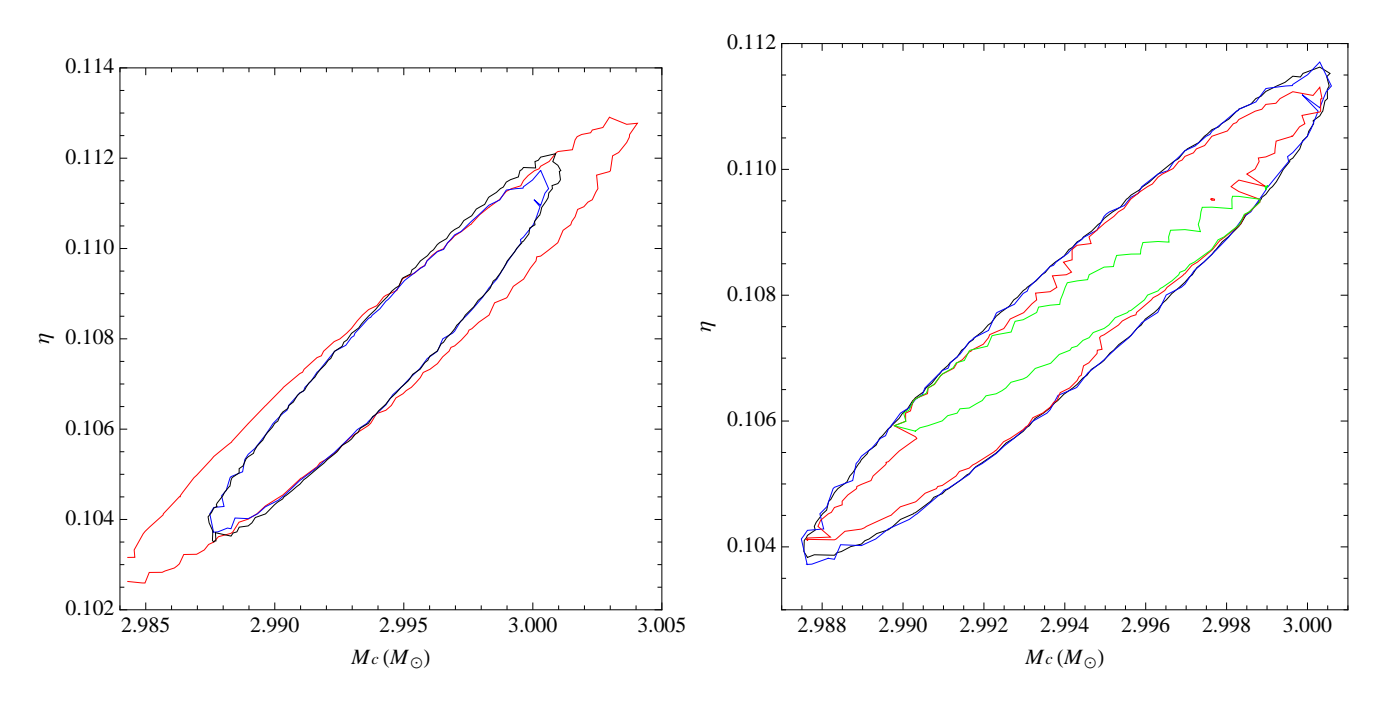


FIG. 8: Marginalized ambiguity contours (where the normalized overlap is 0.99) of intrinsic parameters with various lower limits and sampling rates for the zero spin waveforms with higher harmonics. Left panel: The injected signal starts at 12 Hz and the templates at 12 (black), 30 (blue), and 40 Hz (red). No additional information is added below 30 Hz. Right panel: Contours are calculated by using the sampling rate of 8192 (Black), 4096 (blue), 2048 (red), and 1024 Hz (green) with a fixed starting frequency of 30 Hz. $f_{\text{samp}} \ge 2 \, \text{kHz}$ is required for the zero spin case.

on the following relation:

$$Z(\beta) \equiv \int \mathcal{L}^{\beta} p(\lambda) d\lambda \tag{C2a}$$

$$\frac{d \ln Z}{d\beta} = \frac{1}{Z} \int p(\lambda) \mathcal{L}^{\beta} \ln \mathcal{L} = \langle \ln \mathcal{L} \rangle_{\beta}$$
 (C2b)

$$\ln Z(\beta) = \int_0^\beta d\beta \langle \ln \mathcal{L} \rangle_\beta \tag{C2c}$$

where $\langle X \rangle_{\beta} \equiv \int X \mathcal{L}^{\beta} p(\lambda) d\lambda/Z$. The averages appearing in each integrand can be calculated from each simulations' samples. By definition, the prior

ratio $V/V_{\text{prior}}[\beta]$ can be calculated directly from the temperature-dependent evidence $Z(\beta)$ and the temperature-independent peak likelihoood:

$$\ln(V/V_{\text{prior}})[\beta] = \ln Z(\beta) - \beta \max_{\lambda} \ln \mathcal{L}(\{d\}) \quad (C3)$$

Because the recovered signal amplitude $\rho_{\text{rec}} \equiv \sqrt{2 \max_{\lambda} \ln \mathcal{L}(\{d\})}$ can differ from the zero-noise signal amplitude ρ by a number of order unity, we always calculate the second maximum directly from the samples. Alternatively, this expression can be rewritten as a ther-

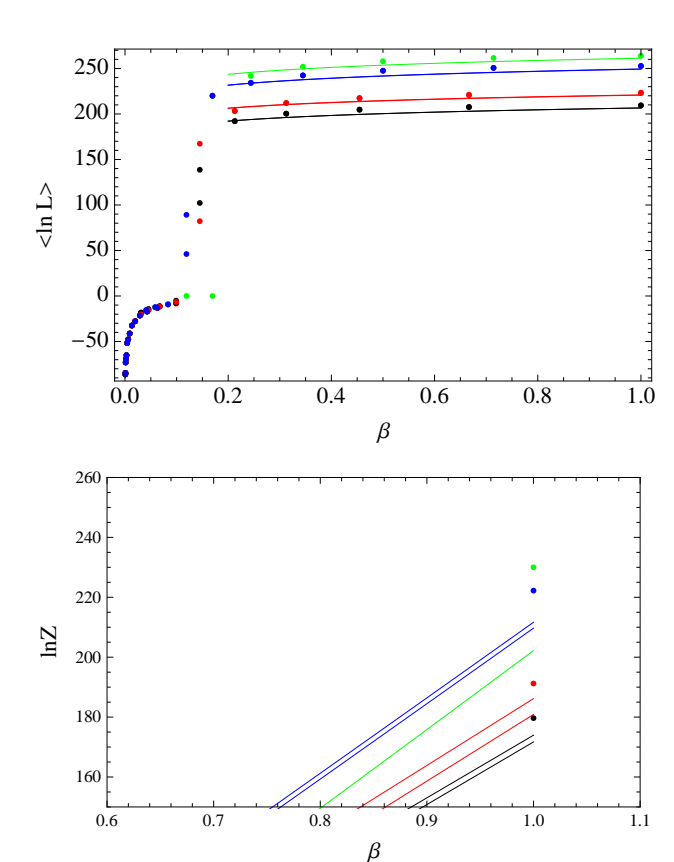


FIG. 9: Thermodynamic integration: Illustration of thermodynamic integration, using samples from zero-noise simulations with zero-spin and no harmonics (black); zero spin and with harmonics (red); aligned spin and no harmonics (blue); and aligned spin with harmonics (green). Top panel: Plot of $\langle \ln \mathcal{L} \rangle_{\beta}$ versus β , a monotonically increasing function needed to compute the thermodynamic integral for the evidence Z [Eq. (C2)]. For comparison, a solid line shows $\rho(\beta)^2/2 + d \ln \rho(\beta)$ where d is the number of parameters (9 or 11) and where $\rho(1)$ is the signal amplitude. Bottom panel: A plot of the derived evidence $\ln Z(\beta)$ versus β derived from the thermodynamic integral using the temperature chains shown above. For comparison, the points show evidence derived from direct integration over the posterior. Direct integration evidence is consistently larger. While the small difference between these two integrals is consistent with discretization error in the thermodynamic integral, associated with in the sharp step in $\langle \mathcal{L} \rangle$ near $\beta \simeq 0.15$, a detailed analysis of the differences between these two evidence calculations is beyond the scope of this work.

modynamic integral:

$$\ln(V/V_{\text{prior}})[\beta] = \int_0^\beta d\beta \langle \ln \mathcal{L}/\mathcal{L}_{\text{max}} \rangle_\beta$$
 (C4)

As a concrete example, the top panel of Figure 9 shows the functional form of the integrand $\langle \ln \mathcal{L} \rangle_{\beta}$ appearing in both thermodynamic expressions for $Z(\beta)$ and V/V_{prior} . The default temperature chain shown in Figure 9 has a sparse temperature grid; to confirm our results and control our error, we have performed followup simulations. Combining the temperature spacing and functional forms

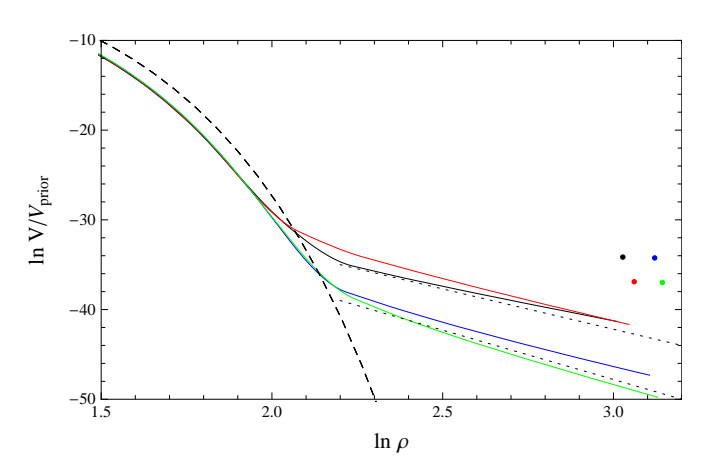


FIG. 10: Prior volume versus amplitude: A plot of $\ln(V/V_{\rm prior})$ versus signal amplitude ρ , derived from the signal amplitude and from $\ln(V/V_{\text{prior}})$ versus β . For comparison, dotted lines are provided with a logarithmic slope -9and -11, the number of parameters in the nonspinning and spinning model, respectively. To illustrate a critical seperatrix between simulation-specific and universal behavior, the dashed line shows the curve $\ln(V/V_{\rm prior}) \simeq -\rho^2/2$ [Eq. (21)]. This curve corresponds to Z = 1: the data is equally consistent with the null hypothesis or the presence of a single signal. For comparison, the dotted and dashed curves intersect at a network amplitude $\rho \simeq \exp 2.1$, roughly consistent with a signal amplitude $\lesssim 5.7$ in each detector. The colored points show the prior volume calculated using the direct integration evidence, as listed in Table III; as in Figure 9, our approximate thermodynamic evidence integral differs from direct integration evidence. The vertical scales' absolute units depend on the choice of prior and have been chosen consistently with all other calculations described in this work.

used here, we expect the thermodynamic evidence to be accurate to within $\Delta \ln Z \lesssim 5$. For small $N_{\rm eff}$, as is often the case for slow simulations, this uncertainty is dominated by chain placement and by slow convergence of the average of $\langle \ln \mathcal{L} \rangle_{\beta}$ near the critical temperatures where this average changes by $\simeq \rho^2/2$.

2. Effective dimension versus amplitude

Each parallel-tempered chain represents a different signal amplitude: using our definition [Eq. (19)],

$$\rho_{\rm rec}(\beta) = \rho_{\rm rec}(1)\sqrt{\beta}$$
 (C5a)

$$\rho(\beta) = \rho(1)\sqrt{\beta} \tag{C5b}$$

Also, from first principles we can calculate the *relative* change $\delta\rho/\rho$ that any physical effect will have on the gravitational wave signal. As a function of temperature, our simulations lose their ability to discriminate between coarser and coarser details, until in the limit $\beta \to 0$ they recover the prior. In other words, the low-temperature chains will probe large amplitude and a large $D_{\rm eff}$ [Eq. (20)]; higher-temperature simulations smooth out fine de-

tails using a lower amplitude $\rho_{\rm rec}$ and may have a significantly lower $D_{\rm eff}$.

The prior volume can be calculated by thermodynamic integration both using the likelihood (above) or the effective dimension [Eq. (20)]:

$$d \ln(V/V_{\text{prior}}) = \langle \ln \mathcal{L}/\mathcal{L}_{\text{max}} \rangle_{\beta} d\beta = -D_{\text{eff}} d \ln \rho \quad (C6)$$

As a concrete example, Figure 10 shows the prior volume versus $\rho(\beta)$. When $\rho(\beta) > 8$, the function $\ln(V/V_{\rm prior})$ is nearly linear versus $\ln \rho$; the slope is $-D_{\rm eff}$. Different physical systems have different numbers of parameters, some of which may not be measurable (e.g., ψ_+). As a result, each curve has a distinct slope at high temperature, set by the number of measurable parameters at $\rho \simeq 10-20$ [Eq. (21)].

At sufficiently high temperatures and low amplitudes, the evidence physically should²¹ converge to nearly equal odds – equivalently, because the signal cannot be distinguished from noise. In this regime, $V/V_{\rm prior}$ follows the dashed line in Figure 10. Below this threshold, the form of $\ln V/V_{\rm prior}$ versus $\ln \rho$ should be universal, set by the definition of the signal amplitude ρ and completely unrelated to the physical dimension of the problem.

- [1] Abbott et al. (The LIGO Scientific Collaboration), Nuclear Instruments and Methods in Physics Research A 517, 154 (2004), arXiv:gr-qc/0308043, URL http://arxiv.org/abs/gr-qc/0308043.
- [2] F. Acernese, P. Amico, M. Alshourbagy, F. Antonucci, S. Aoudia, S. Avino, D. Babusci, G. Ballardin, F. Barone, L. Barsotti, et al., Classical and Quantum Gravity 23, S635 (2006).
- [3] M. Hannam, S. Husa, B. Brügmann, and A. Gopakumar, Phys. Rev. D 78, 104007 (2008).
- [4] A. Buonanno, B. R. Iyer, E. Ochsner, Y. Pan, and B. S. Sathyaprakash, Phys. Rev. D 80, 084043 (2009).
- [5] A. Buonanno, Y. Chen, and M. Vallisneri, Phys. Rev. D 67, 104025 (2003), URL http://arxiv.org/pdf/gr-qc/ 0211087.
- [6] A. Buonanno, Y. Chen, Y. Pan, and M. Vallisneri, Phys. Rev. D 70, 104003 (2004).
- [7] K. G. Arun, A. Buonanno, G. Faye, and E. Ochsner, Phys. Rev. D 79, 104023 (2009).
- [8] Y. Pan, A. Buonanno, Y. Chen, and M. Vallisneri, Phys. Rev. D 69, 104017 (2004), URL http://arxiv.org/abs/gr-qc/0310034.
- [9] T. Damour, A. Gopakumar, and B. R. Iyer, Phys. Rev. D 70, 064028 (2004).
- [10] A. Buonanno, Y. Chen, Y. Pan, H. Tagoshi, and M. Vallisneri, Phys. Rev. D 72, 084027 (2005).
- [11] C. Königsdörffer and A. Gopakumar, Phys. Rev. D 73, 124012 (2006).
- [12] M. Tessmer and A. Gopakumar, MNRAS 374, 721 (2007).
- [13] I. Hinder, F. Herrmann, P. Laguna, and D. Shoemaker, Phys. Rev. D 82, 024033 (2010), 0806.1037.
- [14] C. Königsdörffer and A. Gopakumar, Phys. Rev. D 71, 024039 (2005).

Acknowledgments

The authors appreciate helpful discussions with Madeline Wade, Will Farr, and Tyson Littenburg. This material is based upon work supported by the National Science Foundation Graduate Research Fellowship under Grant No. DGE-0824162 and computing resources supported by the National Science Foundation Major Research Instrumentation Program under Grants No. PHY-0923409 and PHY-1126812. ROS and EO are supported by NSF awards PHY-0970074 and PHY-1307429. H. S. C., C. K., and C. H. L. are supported in part by the National Research Foundation Grant funded from the Korean Government (No. NRF-2011-220-C00029) and in part by the KISTI Global Science Experimental Data Hub Center (GSDC). H. S. C. and C. H. L. are supported in part by the BAERI Nuclear R & D program (No. M20808740002), Korea. C. K. is supported in part by the Research Corporation for Scientific Advancement and by a WVEPSCoR Research Challenge Grant. This work uses computing resources at the KISTI GSDC.

- [15] J. Aasi et al (The LIGO Scientific Collaboration and the Virgo Collaboration), Phys. Rev. D 88, 062001 (2013), URL http://arxiv.org/abs/arXiv:1304.1775.
- [16] W. Del Pozzo, J. Veitch, and A. Vecchio, Phys. Rev. D 83, 082002 (2011).
- [17] N. Cornish, L. Sampson, N. Yunes, and F. Pretorius, Phys. Rev. D 84, 062003 (2011).
- [18] T. G. F. Li, W. Del Pozzo, S. Vitale, C. Van Den Broeck, M. Agathos, J. Veitch, K. Grover, T. Sidery, R. Sturani, and A. Vecchio, Phys. Rev. D 85, 082003 (2012).
- [19] J. Veitch, I. Mandel, B. Aylott, B. Farr, V. Raymond, C. Rodriguez, M. van der Sluys, V. Kalogera, and A. Vecchio, Phys. Rev. D 85, 104045 (2012).
- [20] S. Nissanke, J. Sievers, N. Dalal, and D. Holz, Astrophys. J. 739, 99 (2011).
- [21] J. Veitch, I. Mandel, B. Aylott, B. Farr, V. Raymond, C. Rodriguez, M. van der Sluys, V. Kalogera, and A. Vecchio, Phys. Rev. D 85, 104045 (2012), 1201.1195.
- [22] H. Cho, E. Ochsner, R. O'Shaughnessy, C. Kim, and C. Lee, Submitted to PRD (arXiv:1209.4494) (2012), URL http://arxiv.org/abs/arXiv:1209.4494.
- [23] T. Cokelaer, Classical and Quantum Gravity 25, 184007 (2008).
- [24] M. Vallisneri, Phys. Rev. D 77, 042001 (2008), arXiv:gr-qc/0703086.
- [25] S. Vitale and M. Zanolin, Phys. Rev. D 82, 124065 (2010).
- [26] E. Poisson and C. M. Will, Phys. Rev. D 52, 848 (1995), arXiv:gr-qc/9502040.
- [27] M. Vallisneri, Phys. Rev. D 77, 042001 (2008), URL http://arxiv.org/abs/gr-qc/0703086.
- [28] C. Cutler and E. E. Flanagan, Phys. Rev. D 49, 2658 (1994), gr-qc/9402014.
- [29] C. Van Den Broeck and A. S. Sengupta, Classical and

- Quantum Gravity 24, 155 (2007).
- [30] R. Balasubramanian, B. S. Sathyaprakash, and S. V. Dhurandhar, Phys. Rev. D 53, 3033 (1996), arXiv:gr-qc/9508011.
- [31] V. Raymond, Ph.D. thesis (2012), URL https://gwic. ligo.org/thesisprize/2012/raymond-thesis.pdf.
- [32] E. K. Porter and N. J. Cornish, Phys. Rev. D 78, 064005 (2008).
- [33] R. N. Lang, S. A. Hughes, and N. J. Cornish, Phys. Rev. D 84, 022002 (2011).
- [34] R. N. Lang and S. A. Hughes, Phys. Rev. D 74, 122001 (2006).
- [35] A. Klein, P. Jetzer, and M. Sereno, Phys. Rev. D 80, 064027 (2009).
- [36] A. H. Nitz, A. Lundgren, D. A. Brown, E. Ochsner, D. Keppel, et al. (2013), 1307.1757.
- [37] I. Harry, A. Nitz, D. A. Brown, A. Lundgren, E. Ochsner, et al. (2013), 1307.3562.
- [38] LIGO Scientific Collaboration (LAL source code is available at https://www.lsc-group.phys.uwm.edu/daswg/projects/lalsuite.html, version used dated June, 2013), URL https://www.lsc-group.phys.uwm.edu/daswg/projects/lalsuite.html.
- [39] L. E. Kidder, Phys. Rev. D 52, 821 (1995), arXiv:gr-qc/9506022.
- [40] A. Boh, S. Marsat, and L. Blanchet, Class.Quant.Grav. 30, 135009 (2013), 1303.7412.
- [41] A. Buonanno, G. Faye, and T. Hinderer, Phys.Rev. D87, 044009 (2013), 1209.6349.
- [42] C. M. Will and A. G. Wiseman, Phys. Rev. D 54, 4813 (1996).
- [43] T. Damour, B. R. Iyer, and B. S. Sathyaprakash, Phys. Rev. D 63, 044023 (2001), gr-qc/0010009.
- [44] The LIGO Scientific Collaboration and the Virgo Collaboration, ArXiv e-prints (2010), 1003.2481.
- [45] The LIGO Scientific Collaboration and the Virgo Collaboration, (arXiv:1203.2674) (2012), URL http://arxiv.org/abs/arXiv:1203.2674.
- [46] J. Abadie, B. P. Abbott, R. Abbott, M. Abernathy, T. Accadia, F. Acernese, C. Adams, R. Adhikari, P. Ajith, B. Allen, et al., Classical and Quantum Gravity 27, 173001 (2010), 1003.2480.
- [47] B. J. Owen and B. S. Sathyaprakash, Phys. Rev. D 60, 022002 (1999).
- [48] B. J. Owen, Phys. Rev. D 53, 6749 (1996), URL http://arxiv.org/abs/gr-qc/9511032.
- [49] T. Cokelaer, Phys. Rev. D 76, 102004 (2007), 0706.4437.
- [50] D. A. Brown, I. Harry, A. Lundgren, and A. H. Nitz, (arXiv:1207.6406) (2012), URL http://arxiv.org/abs/ arXiv:1207.6406.
- [51] D. J. C. Mackay, Information Theory, Inference and

- Learning Algorithms (2003).
- [52] U. von Toussaint, Reviews of Modern Physics 83, 943 (2011).
- [53] Burnham and Anderson, Model selection and multimodel inference (Springer, 2002), ISBN 978-0387953649.
- [54] J. Gentle, W. Hardle, and M. Mori, Handbook of Computational Statistics: Concepts and Methods (Berlin: Springer-Verlag, 2004), ISBN 3-540-40464-3.
- [55] J. Skilling, Bayesian Analysis 1, 833 (2006).
- [56] J. Skilling, in American Institute of Physics Conference Series, edited by P. M. Goggans and C.-Y. Chan (2009), vol. 1193 of American Institute of Physics Conference Series, pp. 277–291.
- [57] F. Feroz, M. P. Hobson, and M. Bridges, MNRAS 398, 1601 (2009), 0809.3437.
- [58] P. Ajith, Phys. Rev. D 84, 084037 (2011), 1107.1267.
- [59] D. A. Brown, I. Harry, A. Lundgren, and A. H. Nitz, Phys. Rev. D 86, 084017 (2012), 1207.6406.
- [60] R. O'Shaughnessy, Submitted to PRD (arxiv:1204.3117) (2012), URL http://arxiv.org/abs/1204.3117.
- [61] S. Nissanke, D. E. Holz, S. A. Hughes, N. Dalal, and J. L. Sievers, Astrophys. J. 725, 496 (2010), 0904.1017.
- [62] LIGO Scientific Collaboration, Virgo Collaboration, J. Aasi, J. Abadie, B. P. Abbott, R. Abbott, T. D. Abbott, M. Abernathy, T. Accadia, F. Acernese, et al., ArXiv e-prints (2013), 1304.0670.
- [63] S. Nissanke, M. Kasliwal, and A. Georgieva, Astrophys. J. 767, 124 (2013), 1210.6362.
- [64] E. Poisson, Phys. Rev. D 57, 5287 (1998), arXiv:gr-qc/9709032.
- [65] B. Mikoczi, M. Vasuth, and L. A. Gergely, Phys.Rev. D71, 124043 (2005), astro-ph/0504538.
- [66] G. Faye, L. Blanchet, and A. Buonanno, Phys.Rev. D74, 104033 (2006), gr-qc/0605139.
- [67] L. Blanchet, A. Buonanno, and G. Faye, Phys.Rev. D74, 104034 (2006), gr-qc/0605140.
- [68] M. Hannam, D. A. Brown, S. Fairhurst, C. L. Fryer, and I. W. Harry, ApJL 766, L14 (2013), 1301.5616.
- [69] R. Neal, Statistics and Computing 11, 125 (2001).
- [70] J. Liu, Monte Carlo Strategies in Scientific Computing (New York: Springer, 2001).
- [71] C. Röver, R. Meyer, and N. Christensen, Phys. Rev. D 75, 062004 (2007), gr-qc/0609131.
- [72] M. V. van der Sluys, C. Röver, A. Stroeer, V. Raymond, I. Mandel, N. Christensen, V. Kalogera, R. Meyer, and A. Vecchio, ApJL 688, L61 (2008), 0710.1897.
- [73] T. B. Littenberg and N. J. Cornish, Phys. Rev. D 80, 063007 (2009), 0902.0368.
- [74] V. Raymond, M. V. van der Sluys, I. Mandel, V. Kalogera, C. Röver, and N. Christensen, Classical and Quantum Gravity 26, 114007 (2009), 0812.4302.